The Astrophysical Journal, 974:316 (27pp), 2024 October 20 https://doi.org/10.3847/1538-4357/ad710e

Characterizing the Rapid Hydrogen Disappearance in SN 2022crv: Evidence of a Continuum between Type Ib and IIb Supernova Properties

Yize Dong (董一泽)[1], Stefano Valenti[1], Chris Ashall[2], Marc Williamson[3], David J. Sand[4], Schuyler D. Van Dyk[5], Alexei V. Filippenko[6], Saurabh W. Jha[7], Michael Lundquist[8], Maryam Modjaz[9], Jennifer E. Andrews[10], Jacob E. Jencson[4], Griffin Hosseinzadeh[4], Jeniveve Pearson[4], Lindsey A. Kwok[7], Teresa Boland[7], Eric Y. Hsiao[11], Nathan Smith[4], Nancy Elias-Rosa[12,13], Shubham Srivastav[14], Stephen Smartt[14], Michael Fulton[14], WeiKang Zheng[6], Thomas G. Brink[6], Melissa Shahbandeh[15,16], K. Azalee Bostroem[17,37], Emily Hoang[1], Daryl Janzen[18], Darshana Mehta[1], Nicolas Meza[1], Manisha Shrestha[19], Samuel Wyatt[4], Katie Auchettl[20,21], Christopher R. Burns[22], Joseph Farah[23,24], Lluís Galbany[13,25], Estefania Padilla Gonzalez[23,24], Joshua Haislip[26], Jason T. Hinkle[27,38], D. Andrew Howell[23,24], Thomas De Jaeger[28], Vladimir Kouprianov[26], Sahana Kumar[9], Jing Lu[29], Curtis McCully[23,24], Shane Moran[30], Nidia Morrell[31], Megan Newsome[23,24], Craig Pellegrino[9], Abigail Polin[22,32], Daniel E. Reichart[26], B. J. Shappee[27], Maximilian D. Stritzinger[33], Giacomo Terreran[23,24], and M. A. Tucker[34,35,36,39]

[1] Department of Physics and Astronomy, University of California, 1 Shields Avenue, Davis, CA 95616-5270, USA; yizdong@ucdavis.edu
[2] Department of Physics, Virginia Tech, Blacksburg, VA 24061, USA
[3] Department of Physics, New York University, New York, NY 10003, USA
[4] Steward Observatory, University of Arizona, 933 North Cherry Avenue, Rm. N204, Tucson, AZ 85721-0065, USA
[5] Caltech/IPAC, Mailcode 100-22, Pasadena, CA 91125, USA
[6] Department of Astronomy, University of California, Berkeley, CA 94720-3411, USA
[7] Department of Physics and Astronomy, Rutgers, The State University of New Jersey, 136 Frelinghuysen Road, Piscataway, NJ 08854-8019, USA
[8] W.M. Keck Observatory, 65-1120 Māmalahoa Highway, Kamuela, HI 96743-8431, USA
[9] Department of Astronomy, University of Virginia, Charlottesville, VA 22904, USA
[10] Gemini Observatory, 670 North A'ohoku Place, Hilo, HI 96720-2700, USA
[11] Department of Physics, Florida State University, 77 Chieftan Way, Tallahassee, FL 32306, USA
[12] INAF Osservatorio Astronomico di Padova, Vicolo dell'Osservatorio 5, 35122 Padova, Italy
[13] Institute of Space Sciences (ICE-CSIC), Campus UAB, Carrer de Can Magrans, s/n, E-08193 Barcelona, Spain
[14] Astrophysics Research Centre, School of Mathematics and Physics, Queens University Belfast, Belfast BT7 1NN, UK
[15] Department of Physics and Astronomy, Johns Hopkins University, Baltimore, MD 21218, USA
[16] Space Telescope Science Institute, 3700 San Martin Drive, Baltimore, MD 21218, USA
[17] Department of Astronomy, University of Washington, 3910 15th Avenue NE, Seattle, WA 98195-0002, USA
[18] Department of Physics & Engineering Physics, University of Saskatchewan, 116 Science Place, Saskatoon, SK S7N 5E2, Canada
[19] Steward Observatory, University of Arizona, 933 North Cherry Avenue, Tucson, AZ 85721-0065, USA
[20] School of Physics, The University of Melbourne, Parkville, VIC 3010, Australia
[21] Department of Astronomy and Astrophysics, University of California, Santa Cruz, CA 95064, USA
[22] Observatories of the Carnegie Institution for Science, 813 Santa Barbara Street, Pasadena, CA 91101, USA
[23] Las Cumbres Observatory, 6740 Cortona Drive, Suite 102, Goleta, CA 93117-5575, USA
[24] Department of Physics, University of California, Santa Barbara, CA 93106-9530, USA
[25] Institut d'Estudis Espacials de Catalunya (IEEC), E-08034 Barcelona, Spain
[26] Department of Physics and Astronomy, University of North Carolina, 120 East Cameron Avenue, Chapel Hill, NC 27599, USA
[27] Institute for Astronomy, University of Hawaii, 2680 Woodlawn Drive, Honolulu, HI 96822, USA
[28] CNRS/IN2P3, Sorbonne Université, Université Paris Cité), Laboratoire de Physique Nucléaire et de Hautes Énergies, 75005, Paris, France
[29] Department of Physics and Astronomy, Michigan State University, East Lansing, MI 48824, USA
[30] Tuorla Observatory, Department of Physics and Astronomy, University of Turku, 20014 Turku, Finland
[31] Las Campanas Observatory, Carnegie Observatories, Casilla 601, La Serena, Chile
[32] TAPIR, Walter Burke Institute for Theoretical Physics, 350-17, Caltech, Pasadena, CA 91125, USA
[33] Department of Physics and Astronomy, Aarhus University, Ny Munkegade 120, DK-8000 Aarhus C, Denmark
[35] Center for Cosmology and Astroparticle Physics, The Ohio State University, 191 West Woodruff Avenue, Columbus, OH, USA
[35] Department of Astronomy, The Ohio State University, 140 West 18th Avenue, Columbus, OH, USA
[36] Department of Physics, The Ohio State University, 191 West Woodruff Avenue, Columbus, OH, USA
Received 2023 September 18; revised 2024 July 4; accepted 2024 July 19; published 2024 October 18

Abstract

We present optical and near-infrared (NIR) observations of SN 2022crv, a stripped-envelope supernova in NGC 3054, discovered within 12 hr of explosion by the Distance Less Than 40 Mpc Survey. We suggest that SN 2022crv is a transitional object on the continuum between Type Ib supernovae (SNe Ib) and Type IIb supernovae (SNe IIb). A high-velocity hydrogen feature ($\sim -20{,}000$ to $-16{,}000$ km s^{-1}) was conspicuous in SN 2022crv at early phases, and then quickly disappeared. We find that a hydrogen envelope of $\sim 10^{-3}$ $M_{\odot}$ can

[37] DiRAC Fellow.
[38] FINESST FI.
[39] CCAPP Fellow.

reproduce the observed behavior of the hydrogen feature. The lack of early envelope cooling emission implies that SN 2022crv had a compact progenitor with an extremely low amount of hydrogen. A nebular spectral analysis shows that SN 2022crv is consistent with the explosion of a He star with a final mass of $\sim$4.5–5.6 $M_{\odot}$ that evolved from a $\sim$16 to 22 $M_{\odot}$ zero-age main-sequence star in a binary system with $\sim$1.0–1.7 $M_{\odot}$ of oxygen finally synthesized in the core. In order to retain such a small amount of hydrogen, the initial orbital separation of the binary system is likely larger than $\sim$1000 $R_{\odot}$. The NIR spectra of SN 2022crv show a unique absorption feature on the blue side of the He I line at $\sim$1.005 μm. This is the first time such a feature has been observed in SNe Ib/IIb, and it could be due to Sr II. Further detailed modeling of SN 2022crv can shed light on the progenitor and the origin of the mysterious absorption feature in the NIR.

Unified Astronomy Thesaurus concepts: Supernovae (1668); Type Ib supernovae (1729); Core-collapse supernovae (304)

Materials only available in the online version of record: data behind figures

1. Introduction

Stripped-envelope supernovae (SESNe) are a subclass of core-collapse supernovae (CCSNe) that have partly or completely lost their progenitor envelope prior to their explosions (see M. Modjaz et al. 2019 for a review). SESNe are spectroscopically classified as Type IIb supernovae (SNe IIb), Type Ib supernovae (SNe Ib), and Type Ic supernovae (SNe Ic; R. P. Harkness et al. 1987; J. C. Wheeler & R. P. Harkness 1990; A. Clocchiatti & J. C. Wheeler 1997; A. V. Filippenko 1997), depending on the presence or absence of H and He lines in the optical spectra. SNe Ib show strong He lines but not H lines, while SNe Ic exhibit neither H nor He lines. SNe IIb, first identified by A. V. Filippenko (1988), show clear H lines at early phases, which become weaker over time, and the spectra are similar to those of SNe Ib at late phases. The sequence of SESNe (IIb→Ib→Ic) is commonly believed to result from progenitors experiencing varying extents of envelope stripping (e.g., A. V. Filippenko 1997; S.-C. Yoon 2015; A. Gal-Yam 2017; D. Hiramatsu et al. 2021).

These hydrogen-deficient supernova (SN) progenitors have been suggested to either arise from massive and metal-rich stars undergoing mass loss via stellar winds (S. E. Woosley et al. 1993, 1995, 2002; J. J. Eldridge & C. A. Tout 2004; G. Meynet & A. Maeder 2005; S.-C. Yoon 2017) or from binary interactions (P. Podsiadlowski et al. 1992; S. E. Woosley et al. 1995; S. Wellstein & N. Langer 1999; J. J. Eldridge & C. A. Tout 2004; C. L. Fryer et al. 2007; S. C. Yoon et al. 2010; J. J. Eldridge et al. 2013; S.-C. Yoon et al. 2017; Y. Götberg et al. 2018). Owing to the high observed fraction of SESNe (N. Smith et al. 2011; I. Shivvers et al. 2019), relatively weak stellar winds derived from the X-ray and radio observations (e.g., M. R. Drout et al. 2016), and the small population of very massive stars assuming a Salpeter initial mass function (E. E. Salpeter 1955), most SESN progenitors likely result from lower-mass stars in binary systems. This has been supported by direct imaging of progenitors (G. Aldering et al. 1994; J. R. Maund et al. 2004, 2011; S. D. Van Dyk et al. 2011; J. J. Eldridge et al. 2013; C. Fremling et al. 2014; S. D. Van Dyk et al. 2014; J. J. Eldridge et al. 2015; G. Folatelli et al. 2016; C. D. Kilpatrick et al. 2017; L. Tartaglia et al. 2017; C. D. Kilpatrick et al. 2021), X-ray/radio observations (e.g., S. Wellons et al. 2012; M. R. Drout et al. 2016; D. Brethauer et al. 2022), and relatively low ejecta mass found from SESN light curves (M. R. Drout et al. 2011; J. D. Lyman et al. 2016).

With increasing numbers of well-observed SESNe for each subclass, many objects are becoming difficult to classify unambiguously because they are being discovered with overlapping properties. For instance, an absorption feature at around 6200 Å has been found in some SNe Ib and could be attributed to high-velocity Hα (J. S. Deng et al. 2000; D. Branch et al. 2002; A. Elmhamdi et al. 2006; J. Parrent et al. 2007; M. Stritzinger et al. 2009; S. James & E. Baron 2010; Y.-Q. Liu et al. 2016; S. Holmbo et al. 2023), indicating that these objects may still contain a small amount of hydrogen. However, the 6200 Å features detected in these objects could also be due to Si II λ6355, C II λ6580, or Ne I λ6402 (J. S. Deng et al. 2000; D. Branch et al. 2002; M. Hamuy et al. 2002; M. Stritzinger et al. 2009; M. Tanaka et al. 2009; L. Dessart et al. 2011; S. Hachinger et al. 2012). G. Folatelli et al. (2014) identified a small sample of transitional SNe Ib/c that seem to shift from SNe Ic to SNe Ib over time (although see Y.-Q. Liu et al. 2016). These objects initially show weak helium features with nearly constant velocities during the photospheric phase, suggesting a dense shell in the ejecta. However, the weak hydrogen features seen in these objects technically result in a peculiar SNe IIb classification (although see Y.-Q. Liu et al. 2016, where these objects are reclassified as SNe Ib). D. Milisavljevic et al. (2013) found that SESN 2011ei showed unambiguous hydrogen features at early times but these features quickly disappeared on a timescale of 1 week, suggesting the progenitor retained a thin hydrogen envelope at the time of explosion. Such a transformation is much faster than that observed in typical SNe IIb, which usually occurs on a timescale of months. This implies that some SNe IIb may be misclassified as SNe Ib if they are not caught early enough.

All these observations point toward a continuum between SNe IIb and SNe Ib, which is also supported by theoretical studies. For instance, S. C. Yoon et al. (2010) found that many SN Ib/c progenitors formed in close binary systems are expected to maintain a thin hydrogen layer during their pre-SN stage, producing the high-velocity hydrogen features observed in SNe Ib. In a series of models with various amounts of hydrogen, S. Hachinger et al. (2012) found that if the hydrogen envelope mass at the time of core collapse is between about 0.025 and 0.033 $M_{\odot}$, the difference between SNe Ib and SNe IIb could be unclear.

Although observational evidence has suggested that there is likely a continuum in the amount of helium between SNe IIb and SNe Ib (but see Y.-Q. Liu et al. 2016; C. Fremling et al. 2018; S. Holmbo et al. 2023), whether SNe IIb and SNe Ib can be clearly differentiated observationally is still an open question. To better characterize the classification of different types of SESNe and thus understand their progenitors,

Y.-Q. Liu et al. (2016) performed an analysis of a sample of SESNe. They proposed that the strength of Hα (or the absorption feature around 6200 Å) can be used to differentiate SNe Ib and SNe IIb at all epochs. S. J. Prentice & P. A. Mazzali (2017) reassessed the classification system of SESNe using the spectra of a sample of SESNe and found that there is a clear distinction between He-poor SNe (SNe Ic) and He-rich SNe (SNe Ib/IIb). They attributed the 6200 Å feature in SNe Ib to Hα and further suggested that the He-rich SNe can be split into subgroups based on the profile of the Hα line. To fully utilize spectra taken of SESNe, M. Williamson et al. (2019) proposed a new classification technique based on a support vector machine (SVM). This technique can identify transitional SESNe—that is, SNe that present spectral features resembling more than one SESN subtype—and thus reflect the physical properties of their progenitors. These sample studies imply a gradual transition between SNe Ib and SNe IIb depending on the amount of hydrogen remaining in the progenitor envelope.

To better understand the connections between the different SESN types and the evolution of their progenitors, a sample of SESNe that retains a small amount of hydrogen envelope is required. These objects need to be discovered shortly after the explosion since only the very early-time spectra convey signals from the outer layer of the progenitor star. In this paper, we present optical and infrared data for SN 2022crv, an SESN discovered within ~12 hr of explosion by the Distance Less Than 40 Mpc (DLT40; L. Tartaglia et al. 2018) survey and densely monitored for over 1 yr. As we show in this work, a hydrogen feature is detected in SN 2022crv at early phases, which then quickly disappears shortly after maximum brightness. Detailed analyses suggest that there is very little hydrogen in the SN envelope, making the object a transitional object on the continuum between SNe Ib and SNe IIb.

This paper is organized as follows. The observations of SN 2022crv are presented in Section 2, while the observational properties, such as the reddening, distance, and explosion epoch, are constrained in Section 3. We describe the photometric and spectroscopic properties of SN 2022crv in Sections 4 and 5, respectively. The physical implications of the observations are discussed in Section 6, and we conclude in Section 7.

2. Observations

SN 2022crv/DLT22d was discovered at R.A.(J2000) = $09^{hr}54^{m}25\overset{s}{.}91$, decl.(J2000) = $-25°42'11\overset{''}{.}16$ in the nearby barred spiral (SBc) galaxy NGC 3054 (see Figure 1) on 2022-02-17.20 (Y. Dong et al. (2022), JD 2,459,627.70, r = 18.04 mag), during the course of the DLT40 SN search (L. Tartaglia et al. 2018), utilizing the 0.4 m PROMPT-MO-1 telescope (D. Reichart et al. 2005) at the Meckering Observatory. An earlier detection was recovered in the o-band imaging taken by the Asteroid Terrestrial-Impact Last Alert System (ATLAS; J. L. Tonry 2011; J. L. Tonry et al. 2018; K. W. Smith et al. 2020) on 2022-02-16.99. The object was initially classified as SNe Ib using a spectrum taken with the Gemini Multi-Object Spectrograph (GMOS; I. M. Hook et al. 2004; G. Gimeno et al. 2016) on Gemini North on 2022-02-19.42 (J. E. Andrews et al. 2022). The basic properties of SN 2022crv are summarized in Table 1.

After the discovery, the object was intensely followed by the DLT40 survey using the PROMPT5 and PROMPT-MO telescopes in the *Open* filter and the ATLAS survey in the o and c filters. In addition, high-cadence multiband photometric observations were collected by the worldwide network of robotic telescopes at Las Cumbres Observatory (T. M. Brown et al. 2013) through the Global Supernova Project. Ultraviolet (UV) and optical imaging were taken with the Neil Gehrels Swift Observatory (N. Gehrels et al. 2004) at early times. The object was also followed by the 0.76 m Katzman Automatic Imaging Telescope (KAIT) as part of the Lick Observatory Supernova Search (LOSS; A. V. Filippenko et al. 2001), and the 1 m Nickel telescope at Lick Observatory. B, V, R, and I images of SN 2022crv were obtained with both telescopes, while additional *Clear*-band (close to the R band; see W. Li et al. 2003) images were also obtained with KAIT. The multiband light curves are shown in Figure 2. The reduction process of the photometric data is presented in Appendix A.

Nineteen low-resolution optical spectra were collected with the FLOYDS spectrographs (T. M. Brown et al. 2013) on the 2 m Faulkes Telescopes South and North (FTS and FTN) through the Global Supernova Project. In addition, many optical spectra were obtained with the Robert Stobie Spectrograph (RSS) on the

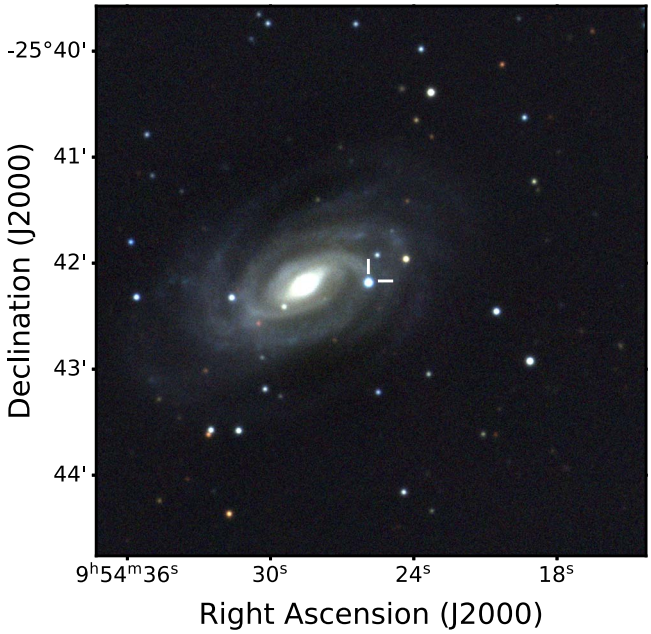

Figure 1. Composite *gri* image of SN 2022crv in NGC 3054 obtained with the Las Cumbres Observatory on 2022 March 4. The position of SN 2022crv is indicated by white tick marks.

Table 1
Basic Properties of SN 2022crv

Parameter	Value
Host galaxy	NGC 3054
R.A. (J2000)	$09^{hr}54^{m}25\overset{s}{.}91$
Decl. (2000)	$-25°42'11\overset{''}{.}16$
Distance	$31.6^{+6.4}_{-5.3}$ Mpc
Distance modulus	32.5 ± 0.4 mag
Redshift z	0.008091 ± 0.000023
$E(B-V)_{MW}$	$0.0642^{+0.007}_{-0.007}$ mag[a]
$E(B-V)_{host}$	$0.146^{+0.009}_{-0.009}$ mag
Explosion epoch (JD)	2, 459,627.19 ± 0.30 (2022-02-16)
V_{max} (JD)	2,459,645.42 ± 0.30 (2022-03-06)

Note.
[a] E. F. Schlafly & D. P. Finkbeiner (2011).

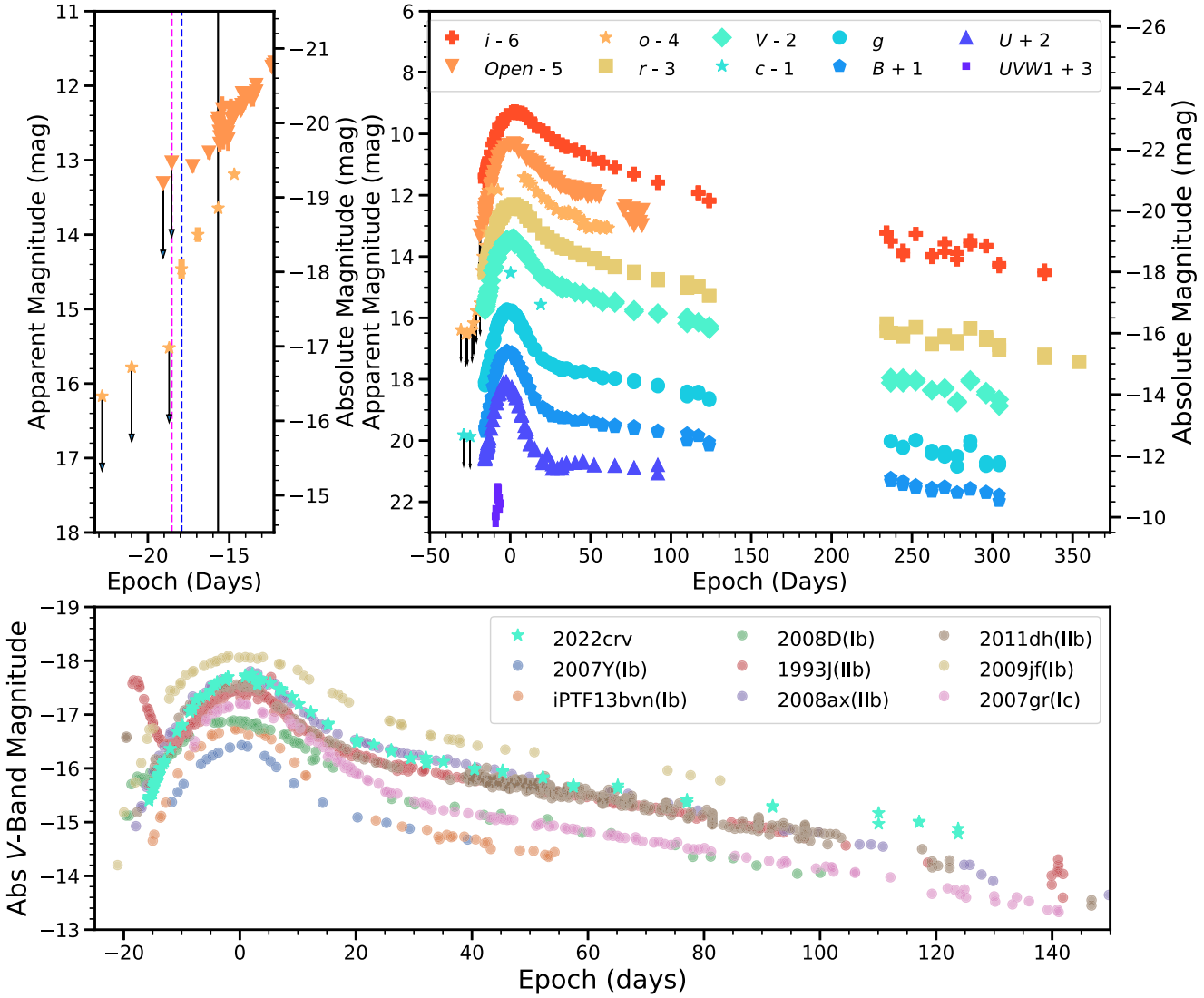

Figure 2. Upper right: multiband light curves of SN 2022crv with respect to the time of *V*-band maximum brightness (JD 2,459,645.42). The marker size is larger than the uncertainties. The DLT40 *Open* filter light curve is calibrated to the *r* band. Upper left: a zoom around a few days before and after the discovery. Only the *Open*- and *o*-band light curves are plotted here to show the constraint on the explosion epoch. The last nondetection and the earliest detection are marked by the magenta vertical dashed line and blue vertical dashed line, respectively. The black vertical line marks when the multiband follow-up observations began. Bottom: the absolute *V*-band light curve of SN 2022crv compared with that of other SESNe. The multiband photometry of SN 2022crv is available in machine readable format as the data behind the Figure. (The data used to create this figure are available in the online article.)

Southern African Large Telescope (SALT; M. P. Smith et al. 2006), the Kast spectrograph on the 3 m Shane telescope (J. S. Miller & R. P. S. Stone 1994) at Lick Observatory, the Boller & Chivens Spectrograph (B&C) on the Bok Telescope (R. Green et al. 1995), one of the Multi-Object double Spectrographs (R. W. Pogge et al. 2010) on the Large Binocular Telescope (LBT), the Binospec instrument on the MMT (D. Fabricant et al. 2019), the Goodman High Throughput Spectrograph on the Southern Astrophysical Research Telescope (SOAR; J. C. Clemens et al. 2004), the Low-Resolution Imaging Spectrometer (LRIS; J. B. Oke et al. 1995) on the 10 m Keck I telescope, the GMOS (I. M. Hook et al. 2004; G. Gimeno et al. 2016) on the Gemini North telescope, the Andalucia Faint Object Spectrograph and Camera (ALFOSC) on the Nordic Optical Telescope (NOT) as part of the NOT Unbiased Transients Survey 2 Collaboration,[40] the SuperNova Integral Field Spectrograph (SNIFS; B. Lantz et al. 2004) mounted at the University of Hawaii 2.2 m telescope (UH88) at Maunakea as part of the Spectroscopic Classification of Astronomical Transients survey (M. A. Tucker et al. 2022), the Inamori-Magellan Areal Camera & Spectrograph (IMACS; A. Dressler et al. 2011) on the 6.5 m Magellan Baade telescope as part of the Precision Observations of Infant Supernova Explosions (POISE; C. Burns et al. 2021), the Optical System for Imaging and low/intermediate-Resolution Integrated Spectroscopy (OSIRIS; J. Cepa et al. 2000) spectrograph on the 10.4 m Gran Telescopio Canarias (GTC), and the Low-Dispersion Survey Spectrograph 3 (LDSS3, which was updated from LDSS2; J. Allington-Smith et al. 1994) on the 6.5 m Magellan Clay telescope.

Near-infrared (NIR) spectra were taken with the Near-Infrared Echellette Spectrometer (NIRES; J. C. Wilson et al. 2004) on the 10 m Keck II telescope, the Folded-port InfraRed Echellette (FIRE; R. A. Simcoe et al. 2013) on the Magellan

[40] https://nuts.sn.ie

Table 2
Spectroscopic Observations of SN 2022crv

Phase[a] (days)	MJD	Telescope	Instrument	Range (Å)
−15.5/2.7	59629.43	Gemini-N	GMOS	3760–7030
−15.5/2.8	59629.46	Keck II	NIRES	9650–24660
−15.3/2.9	59629.61	FTS	FLOYDS	4850–10170
−15.1/3.1	59629.82	SALT	RSS	3930–7790
−13.4/4.8	59631.49	FTN	FLOYDS	3510–9990
−11.5/6.7	59633.39	FTN	FLOYDS	3510–9990
−10.7/7.5	59634.23	SOAR	Goodman	3780–5460
−10.5/7.8	59634.46	FTN	FLOYDS	3500–9990
−7.6/10.6	59637.34	FTN	FLOYDS	3510–10000
−6.6/11.6	59638.32	LBT	MODS	3400–10100
−6.5/11.8	59638.46	FTN	FLOYDS	3510–9990
−3.5/14.7	59641.43	FTS	FLOYDS	3510–9990
−0.6/17.7	59644.35	FTN	FLOYDS	3500–9990
2.3/20.5	59647.22	Bok	B&C	4010–7490
2.7/21.0	59647.65	FTS	FLOYDS	3500–9990
3.4/21.6	59648.29	LBT	MODS	3610–10290
4.4/22.6	59649.28	FTN	FLOYDS	3500–9990
4.4/22.6	59649.32	UH88	SNIFS	3410–9090
6.2/24.4	59651.07	Baade	FIRE	7910–25250
6.4/24.6	59651.34	FTN	FLOYDS	3500–9990
6.6/24.8	59651.50	Baade	IMACS	4230–9410
7.4/25.7	59652.34	Keck II	NIRES	9650–24660
8.3/26.6	59653.27	Keck II	NIRES	9660–24670
10.4/28.6	59655.30	FTN	FLOYDS	3500–10000
12.1/30.3	59657.00	MMT	MMIRS	9500–24290
12.4/30.6	59657.32	UH88	SNIFS	3410–9090
15.6/33.8	59660.50	Baade	IMACS	4230–9410
15.7/33.9	59660.60	FTS	FLOYDS	3510–9500
17.3/35.6	59662.25	Shane	Kast	3620–10750
18.3/36.5	59663.19	LBT	MODS	3400–9990
19.2/37.5	59664.17	MMT	Binospec	5240–6750
19.3/37.6	59664.25	UH88	SNIFS	3410–9090
24.0/42.2	59668.90	NOT	ALFOSC	3410–9660
24.6/42.8	59669.50	Baade	IMACS	4230–9410
25.3/43.5	59670.21	Shane	Kast	3630–10740
28.6/46.9	59673.57	FTS	FLOYDS	3510–9990
35.4/53.6	59680.28	FTN	FLOYDS	3500–9990
35.4/53.6	59680.29	UH88	SNIFS	3410–9090
36.6/54.8	59681.50	Baade	IMACS	4230–9410
44.6/62.9	59689.54	FTS	FLOYDS	3500–10000
48.4/66.6	59693.29	UH88	SNIFS	3410–9090
50.3/68.6	59695.24	Keck I	LRIS	3150–5640
50.3/68.6	59695.24	Keck I	LRIS	5420–10300
50.3/68.6	59695.25	Keck I	LRIS	5490–7140
54.9/73.2	59699.86	SALT	RSS	3930–7790
56.5/74.7	59701.42	FTS	FLOYDS	3500–10000
58.2/76.5	59703.15	LBT	MODS	3720–10000
64.4/82.6	59709.29	Keck II	NIRES	9660–24670
69.3/87.6	59714.25	Keck II	NIRES	9650–24670
70.3/88.6	59715.25	Keck II	NIRES	9660–24670
71.5/89.7	59716.43	FTS	FLOYDS	3500–9990
99.5/117.7	59744.41	FTS	FLOYDS	4010–10000
102.8/121.0	59747.73	SALT	RSS	3930–7790
267.4/285.6	59912.29	SOAR	Goodman	3500–7130
272.3/290.6	59917.27	SOAR	Goodman	5000–9000
321.0/339.2	59965.90	SALT	RSS	5480–8990
353.2/371.4	59998.14	Clay	LDSS3	4000–10000
355.1/373.3	60000.03	GTC	OSIRIS	4000–10000

Note.
[a] Phase is measured relative to the dates of V_{max}/explosion.

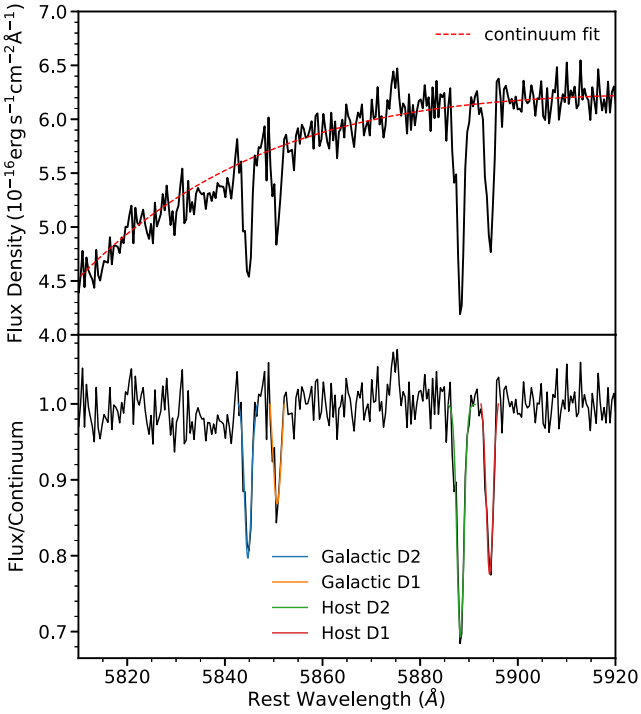

Figure 3. Top: a high-resolution spectrum taken with LRIS 50.3 days after the maximum light showing the Na I D lines from the host galaxy and the Milky Way. The continuum is fit with a fourth-order polynomial function. Bottom: the continuum-normalized spectrum. The Na I D lines are fitted with Gaussian functions using an MCMC routine.

Baade telescope, and the MMT and Magellan Infrared Spectrograph (MMIRS) on the MMT (B. McLeod et al. 2012).

A log of the spectroscopic observations is given in Table 2. The reduction process for the spectroscopic data is presented in Appendix B.

3. Observational Properties

3.1. Explosion Epoch

By combining the early light curves from the DLT40 and ATLAS surveys, we are able to put a strong constraint on the explosion date of SN 2022crv. The SN was not detected during the DLT40 search on JD 2,459,626.89 (with a 5σ limit of 18.03 mag). On JD 2,459,627.49, ∼14.4 hr after our nondetection, the SN was detected in an *o*-band ATLAS image. The first detection and the last nondetection of SN 2022crv are highlighted in the left panel of Figure 2. By taking the average between the first detection and the last nondetection, we constrain the explosion epoch to be JD 2,459,627.19±0.30, which will be adopted throughout the paper.

3.2. Reddening Estimation

The equivalent width (EW) of the Na I D line is often used to estimate the SN reddening with the assumption that it is a good tracer of the amount of gas and dust along the line of sight (e.g., U. Munari & T. Zwitter 1997; D. Poznanski et al. 2012). In order to measure the line-of-sight reddening toward SN 2022crv, we analyze the medium-resolution spectrum ($R \approx 4000$) taken with LRIS on 2022 April 26 (Figure 3). We apply a fourth-order polynomial to fit the continuum, and measure the EW of the Na I D lines on the continuum-normalized spectrum (Figure 3 bottom panel). The measured

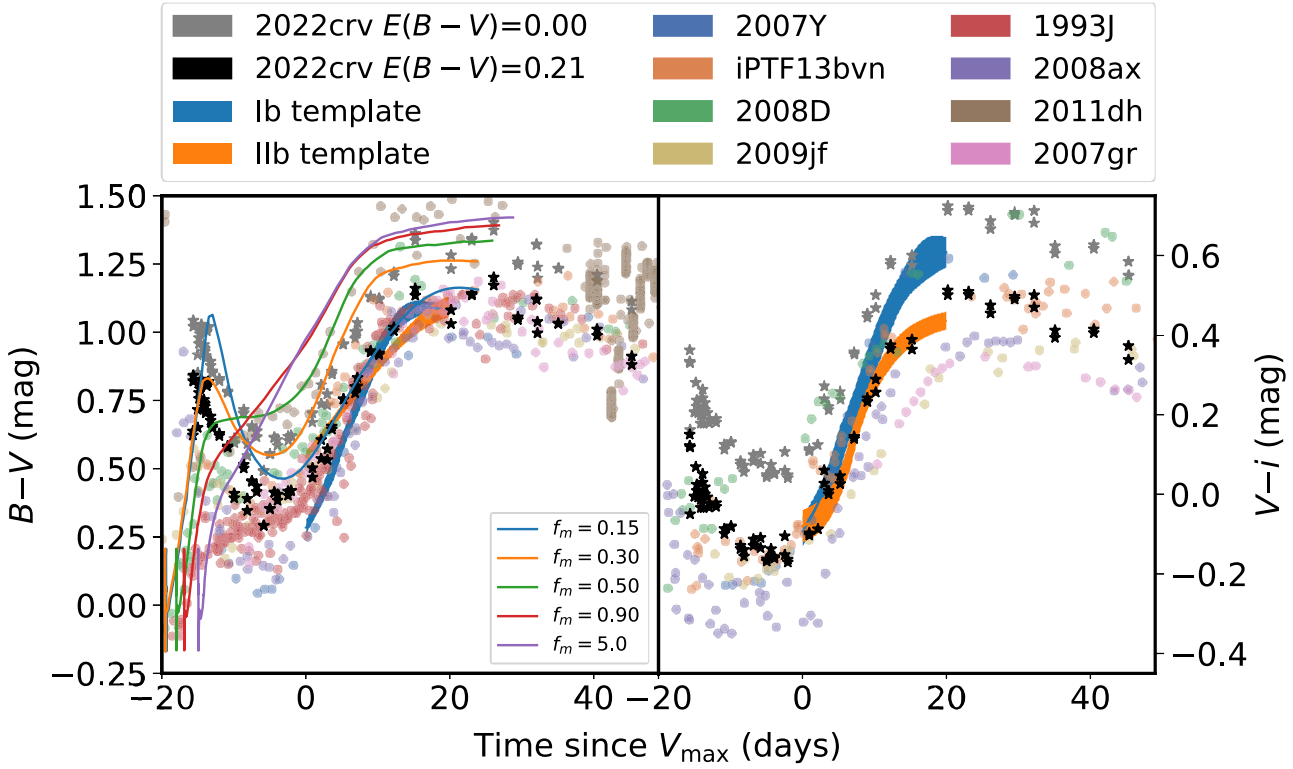

Figure 4. Color evolution of SN 2022crv, after correcting for a total color excess of $E(B-V)=0.21$ mag. The color templates are from M. D. Stritzinger et al. (2018). A sample of SNe Ib/IIb after correcting with the published reddening estimates is also plotted. In addition, the $B-V$ color evolution is compared with the SNe Ib color evolution models by S.-C. Yoon et al. (2019) with various degrees of ^{56}Ni (indicated by f_m). SN 2022crv is more consistent with the $f_m=0.15/0.3$ model, suggesting relatively weak ^{56}Ni mixing in the ejecta (see Section 4).

EW of the host galaxy Na I D λ5890 (D_2) and Na I D λ5896 (D_1) are $0.544^{+0.012}_{-0.012}$ Å and $0.378^{+0.011}_{-0.011}$ Å, respectively. The measured EW of the Galactic Na I D_2 and Na I D_1 are $0.404^{+0.011}_{-0.011}$ Å and $0.247^{+0.011}_{-0.011}$ Å, respectively. Using Equation (9) of D. Poznanski et al. (2012) and applying the renormalization factor of 0.86 from E. F. Schlafly et al. (2010), we found a host extinction of $E(B-V)_{\rm host}=0.146^{+0.009}_{-0.009}$ mag with 20% systematic uncertainty (D. Poznanski et al. 2012). The Milky Way extinction is measured to be $E(B-V)_{\rm MW}=0.070^{+0.004}_{-0.004}$ mag, consistent with the value from E. F. Schlafly & D. P. Finkbeiner (2011) of $E(B-V)_{\rm MW}=0.0642(0.0007)$ mag. The latter will be adopted in this paper.

For SESNe, the intrinsic color shortly after maximum light is found to be tightly distributed, both observationally (M. R. Drout et al. 2011; F. Taddia et al. 2015; M. D. Stritzinger et al. 2018) and theoretically (L. Dessart et al. 2016; S. E. Woosley et al. 2021). By studying a sample of SESNe, M. R. Drout et al. (2011) and M. D. Stritzinger et al. (2018) found that, compared to other phases, the scatter in various color indices for each subtype of SESN is smaller shortly after maximum brightness. Based on the modeling of a range of SESNe, S. E. Woosley et al. (2021) confirmed that there are pinches in color indices shortly after the peak. They also found that the model spectra of SESNe are similar to each other $\sim$10 days after the peak.

In the top panel of Figure 4, we compare the $B-V$ and $V-i$ evolution of SN 2022crv with those of other well-studied SESNe, including SN 2009jf (D. K. Sahu et al. 2011; S. Valenti et al. 2011), SN 2007Y (M. Stritzinger et al. 2009), SN 2008D (M. Modjaz et al. 2009), SN 1993J (A. V. Filippenko et al. 1993), SN 2008ax (A. Pastorello et al. 2008), SN 2011dh (M. Ergon et al. 2014), iPTF13bvn (C. Fremling et al. 2014), and SN 2007gr (D. J. Hunter et al. 2009). These objects have been selected because they are SESNe that are among the best, well-sampled light curves and spectral sequences in literature; they cover the very early phases up to the nebular phases, making them suitable as a comparison sample. As we will show in Section 4, the peak brightness of each object collectively spans a wide range, representing the diversity of SESNe. The color templates for SNe Ib and IIb from M. D. Stritzinger et al. (2018) are also plotted. We found that a total extinction of $E(B-V)=0.21$ mag gives SN 2022crv a consistent color evolution with our comparison sample of SNe Ib/IIb and templates shortly after $V_{\rm max}$. In the bottom panel of Figure 4, we compare the spectrum of SN 2022crv with the other SNe Ib/IIb at $\sim$10 days after $V_{\rm max}$. The original spectrum of SN 2022crv is redder than that of our other objects, while a total extinction of $E(B-V)=0.21$ mag gives a spectral slope more consistent with the population. Therefore, throughout this paper, we will adopt an $E(B-V)_{\rm tot}=0.21$ mag, assuming $R_V=3.1$.

3.3. Distance

The distance of NGC 3054 listed in the NASA/IPAC Extragalactic Database (NED) ranges from 12.9 to 40.0 Mpc. SN 2006T (SNe IIb) (L. A. G. Monard 2006) also exploded in NGC 3054, and J. D. Lyman et al. (2016) used a distance of 32.9 Mpc for SN 2006T, while F. Taddia et al. (2018) adopted a distance of 31.6 Mpc. To be consistent with the distance of SN 2006T used by previous works, we assume a distance of $31.6^{+6.4}_{-5.3}$ Mpc (a distance modulus of 32.5 ± 0.4 mag) based on the Tully–Fisher distance (R. B. Tully et al. 2009).

Table 3
Oxygen Abundance from Diagnostics of M. Curti et al. (2020)[a]

Indicator	Line Ratio	Value	12 + log[O/H]
R3	[O III] λ5007/Hβ	0.13	8.84 ± 0.07
N2	[N II] λ6583/Hα	0.39	8.75 ± 0.10
S2	[S II] $\lambda\lambda$ 6717, 6731/Hα	0.18	8.87 ± 0.06
RS_{32}	[O III] λ5007/Hβ + [S II] λ6717, 6731/Hα	0.31	8.85 ± 0.08
O_3S_2	([O III] λ5007/Hβ) / ([S II] $\lambda\lambda$ 6717, 6731/Hα)	0.72	8.76 ± 0.11
O_3N_2	([O III] λ5007/Hβ) / ([N II] λ6583/Hα)	0.34	8.84 ± 0.09
Weighted Average			8.83 ± 0.08

Note.
[a] Emission line fluxes at the SN position were measured from the spectrum taken on 2023 March 23 (371 days after the explosion).

3.4. Host-galaxy Properties

SN 2022crv is at a projected offset of $36\farcs4$ ($5.6^{+1.1}_{-0.9}$ kpc) from the host galaxy NGC 3054. To estimate the metallicity at the SN position, we measured the flux of the strong ionized gas emission lines (Hβ, [O III] λ5007, [N II] λ6583, Hα, [S II] $\lambda\lambda$ 6717, 6731) from the spectrum taken 371.5 days after the SN explosion. The continuum is removed by fitting a linear component around the narrow emission lines. By using the strong-line diagnostics presented by M. Curti et al. (2020), the weighted average oxygen abundance at the SN site is measured to be $12 + \log(\mathrm{O/H}) = 8.83 \pm 0.08$ and the results for each indicator calibration are shown in Table 3. We note that the different diagnostics are not fully independent, so the weighted average value provided here is calculated solely for reference. Assuming a solar oxygen abundance of $12 + \log(\mathrm{O/H}) = 8.69$ (C. Allende Prieto et al. 2001) as well as a solar metallicity ($Z_\odot$) of 0.0134 (M. Asplund et al. 2009), $12 + \log(\mathrm{O/H}) = 8.83$ is equivalent to a metallicity of $Z \approx 1.4\ Z_\odot \approx 0.019$. The O_3N_2 calibration indicator of M. Pettini & B. E. J. Pagel (2004) gives $12 + \log(\mathrm{O/H}) = 8.88 \pm 0.14$, consistent with our measurements above. Compared to all the SESNe in the PMAS/PPak Integral-field Supernova Hosts Compilation (PISCO) sample (L. Galbany et al. 2018), SN 2022crv has one of the most metal-rich environments among the SNe Ib/IIb in the sample. Given the high metallicity, the progenitor star of SN 2022crv likely experienced strong wind mass loss (J. S. Vink et al. 2001; M. R. Mokiem et al. 2007; P. A. Crowther 2007). Just before completing our paper, another paper on SN 2022crv appeared (A. Gangopadhyay et al. 2023), finding a high progenitor mass-loss rate based on the radio light curve, consistent with what we suggest here. The implication of the high mass-loss rate will be further discussed in Section 6.3.2.

4. Photometric Evolution

4.1. Light-curve Evolution

The multiband light curves of SN 2022crv are shown in Figure 2. SN 2022crv reaches a V-band maximum of $M_V = -17.7 \pm 0.4$ mag on JD 2,459,645.42, ~18.2 days after the date of explosion. Around 60 days after $V_{\max}$, the light curves show a linear (in mag) decline. The V-band decline rate is about 1.4 mag(100 days)$^{-1}$, faster than the expected radioactive decay rate of $^{56}\mathrm{Co} \rightarrow {}^{56}\mathrm{Fe}$ [0.98 mag(100 days)$^{-1}$] (D. K. Nadyozhin 1994), consistent with other SNe Ib/IIb. In the bottom panel of Figure 2, we compare the V-band light curve of SN 2022crv with that of other well-studied SESNe (SNe Ib—SN 2007Y (M. Stritzinger et al. 2009), iPTF13bvn (C. Fremling et al. 2014), SN 2008D (M. Modjaz et al. 2009), SN 2009jf (S. Valenti et al. 2011); SNe IIb—SN 1993J (A. V. Filippenko et al. 1993), SN 2008ax (A. Pastorello et al. 2008), SN 2011dh (M. Ergon et al. 2014); and SN Ic—SN 2007gr (D. J. Hunter et al. 2009)). The reason for choosing these objects for comparison is described in Section 3.2. As shown in the bottom panel of Figure 2, the objects span a wide range of magnitudes, making them a good representative sample of SESNe.

We choose the V band for comparison because all of the objects have coverage in V light curves. SN 2022crv does not show an initial peak due to shock cooling like SN 1993J does, and it has a faster rise than SN 2008D. Overall, however, the light-curve shape of SN 2022crv is similar to that of other SESNe.

R. A. Chevalier & A. M. Soderberg (2010) suggested that SNe IIb can be divided into two categories according to whether the progenitor is compact or extended. If the amount of hydrogen is sufficiently low, the compact Type IIb would merge into SNe Ib. Owing to the absence of cooling envelope emission, SN 2022crv likely has a compact progenitor, which will be further discussed in Section 6.2.

The $B - V$ and $V - i$ color evolution of SN 2022crv are compared to our sample of SNe Ib/IIb in Figure 4. The color evolution of SN 2022crv after $V_{\max}$ is similar to that of other comparison SESNe. After correcting for reddening, the $B - V$ color of SN 2022crv shows a rapid initial rise and reaches a peak of ~0.8 mag. The color then evolves toward the blue down to ~0.4 mag. After maximum light, the $B - V$ color increases and reaches a peak of ~1.1 mag before entering the nebular phase. The $V - i$ color of SN 2022crv shows a similar trend. Through hydrodynamical simulations, S.-C. Yoon et al. (2019) found that the early color evolution of SNe Ib/c is strongly affected by the ^{56}Ni mixing level in the SN ejecta. The ^{56}Ni mixing level is characterized by f_m by S.-C. Yoon et al. (2019), with a larger value of f_m representing more extensive mixing. The $B - V$ evolution of SN 2022crv matches with the $f_m = 0.15$ or the $f_m = 0.3$ model presented by S.-C. Yoon et al. (2019) (Figure 4), implying weak ^{56}Ni mixing in SN 2022crv.

4.2. Bolometric Light Curve

In this section, we build the bolometric light curve of SN 2022crv, which will be used to determine the physical parameters of the explosion in Section 6.3.4.

We calculate the bolometric light curve by fitting the reddening-corrected spectral energy distribution (SED) of SN 2022crv with a blackbody spectrum at each epoch using a Markov Chain Monte Carlo (MCMC) routine in the Light Curve Fitting package (G. Hosseinzadeh & S. Gomez 2020). The bolometric light curve of SN 2022crv is shown in Figure 5 alongside ones from a sample of SNe Ib/IIb. The same method was employed to derive the bolometric light curves for objects in the comparison sample. The peak bolometric luminosity of SN 2022crv is 3.6×10^{42} erg s^{-1}, which places SN 2022crv at the more luminous end among other SNe Ib/IIb (J. D. Lyman et al. 2016; F. Taddia et al. 2018; S. J. Prentice et al. 2019).

From the blackbody fits, we also derived the radius and temperature evolution of SN 2022crv (bottom panel of

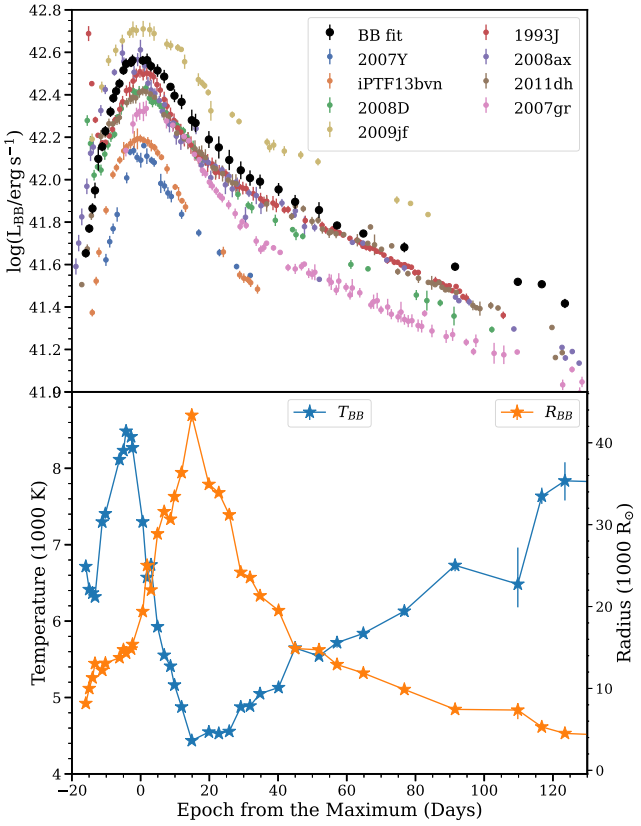

Figure 5. Top: bolometric light curve of SN 2022crv compared with other SNe Ib/IIb. The unfilled points represent the bolometric light curve from the blackbody fit. Bottom: The evolution of temperature and radius of SN 2022crv derived from the blackbody fit.

Figure 5). The temperature initially drops rapidly at early phases, then increases, peaking at ∼8500 K several days before $V_{\rm max}$ and subsequently decreasing rapidly until reaching a minimum of about 4500 K before the object settles into the nebular phase. The behavior of the temperature evolution is consistent with the color evolution shown in Figure 4. The radius of SN 2022crv continuously increases until it peaks around 20 days after $V_{\rm max}$. The radius and temperature evolution of SN 2022crv are similar to those of other SESNe (F. Taddia et al. 2018).

5. Spectroscopic Evolution

5.1. Evolution of Optical Spectra

The optical spectra from the photospheric to the early nebular phase are shown in Figure 6. The early-time spectra show a prominent absorption line at ∼6200 Å, which could be due to Si II or high-velocity Hα. We also note that a small notch appears at 4595 Å at early phases (marked in Figure 6) and could arise from Hβ at a velocity similar to that of Hα. We will discuss the ∼6200 Å absorption line further in Section 6.2. He I λ5876 appears in the first spectrum and its EW gets larger over time. He I λ6678, He I λ7065, and He I λ7281 can be seen after −6.6 days. The Fe II λ4561, Fe II λ5018, and Fe II λ5169 lines, which are good tracers of photospheric velocity (e.g., L. Dessart & D. J. Hillier 2005), can be identified after −11.5 days. Other typical lines seen in SESNe, such as Ca II H&K λλ3934, 3969, Ca II λλ 8498, 8542, 8662, and O I λ7774, are strong before the object is well into the nebular phase. The [Ca] II λλ 7291, 7323 and [O I] λλ 6300, 6364 doublets start to emerge after day 35.4 and dominate the late-phase (⩾100 days) spectra. The evolution of the velocities of He I λ5876, He I λ6678, Fe II λ4561, Fe II λ5018, and Fe II λ5169 are shown in Figure 7. The velocity evolution of the 6200 Å line is also shown in Figure 7, assuming it is from Hα. The positions of the flux minima of these lines are listed in Tables 4 and 5.

In Figure 8, we compare the optical spectra of SN 2022crv at day −15.5, day −10.5, day −0.6, and day +15.7 with those of other SESNe at similar epochs, including SNe Ib 2007Y (M. Stritzinger et al. 2009), iPTF13bvn (C. Fremling et al. 2014), 2008D (M. Modjaz et al. 2009; M. Tanaka et al. 2009), and 2009jf (D. K. Sahu et al. 2011; S. Valenti et al. 2011); SNe IIb 1993J (A. V. Filippenko et al. 1993), 2008ax (A. Pastorello et al. 2008), and 2011dh (M. Ergon et al. 2014); and SN Ic 2007gr (D. J. Hunter et al. 2009). We note that SN 2009jf is a He-weak SN Ib (S. Valenti et al. 2011), making its spectra more indicative of a transitional object between SNe Ib and Ic. At early phases, SN 2022crv is more similar to the SNe IIb in our comparison sample; however, after maximum light, SN 2022crv closely resembles the SN Ib sample. The 6200 Å feature in SN 2022crv completely disappeared around 15 days after $V_{\rm max}$, while the Hα line in SNe IIb is still strong at similar phases. This will be discussed further in Section 6.2.

5.2. Nebular Spectra

The nebular spectra are shown in Figure 9. In Figure 10, we compare the nebular spectra of SN 2022crv with those of other SNe Ib/IIb at similar epochs, finding that in agreement with the sample, SN 2022crv is dominated by strong [O I] λλ 6300, 6364 and [Ca II] λλ 7291, 7323. In addition, weak Mg I] λ4571 and the Na I D doublet can be seen in the spectra. The hydrogen emission is nonexistent or very weak, further supporting that SN 2022crv has a compact progenitor (R. A. Chevalier & A. M. Soderberg 2010).

The [O I] and [Ca II] lines are often used to constrain the progenitor masses of SESNe, so a detailed analysis is presented in Figure 11. The [O I] doublet is slightly blended with [N II] λλ 6548, 6583, and the [Ca II] line is blended with He I λ7065 and [Fe II] λ7155. In order to deblend [O I] and [Ca II] from other lines, we fit two Gaussians around each of [O I] and [Ca II]. The continuum is defined by a line segment connecting the two local minima. The nebular spectrum has been scaled to the *r*- and *i*-band photometry, and the fits are shown in Figure 11. The flux of [O I] at day 290.3 is measured to be 2.9×10^{-14} erg s^{-1} cm^{-2}, and the [O I]/[Ca II] flux ratio is found to be 1.5. At day 371.3, the [O I]/[Ca II] flux ratio is 1.6, consistent with the value we obtained at 290.3 days. In Section 6.3.2, these measurements will be used to constrain the progenitor properties of SN 2022crv.

5.3. Evolution of NIR Spectra

Figure 12 shows the NIR spectroscopic evolution of SN 2022crv. The first spectrum was taken only ∼2.8 days after the explosion, and it shows a prominent absorption line on the blue side. If we attribute this line to He I λ1.083 μm, the velocity would be ∼26,000 km s^{-1}, based on the minimum of the absorption. In Figure 13, we compare the combined optical and NIR spectrum of SN 2022crv with that of other SESNe at various epochs, including SNe Ib 2008D (M. Modjaz et al.

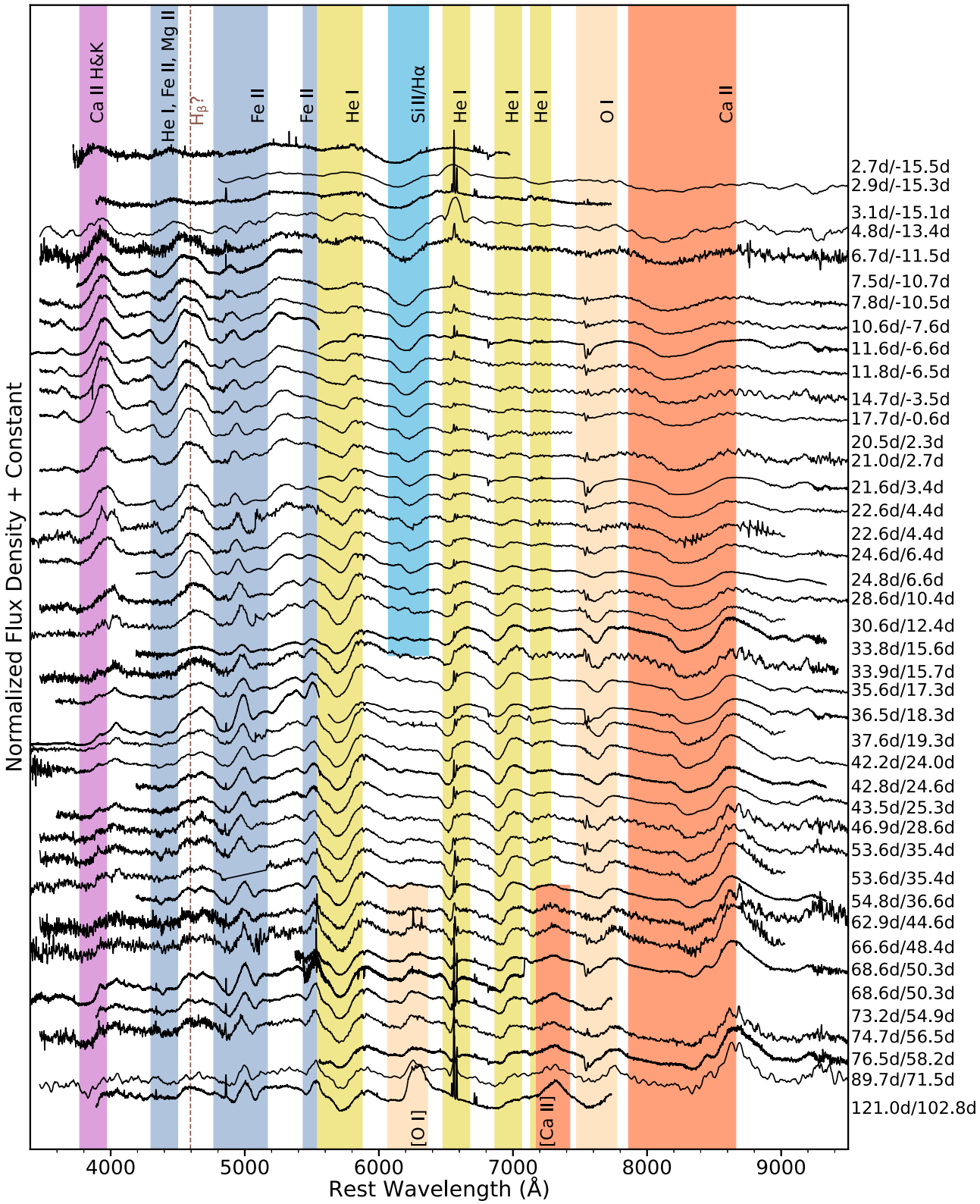

Figure 6. The optical spectroscopic evolution of SN 2022crv from the photospheric phase to the early nebular phase. The phase is measured from the dates of explosion and *V*-band maximum. These spectra are available in machine readable format at the data behind the figure.
(The data used to create this figure are available in the online article.)

2009), 2009jf (S. Valenti et al. 2011), and iPTF13bvn (C. Fremling et al. 2014); and SNe IIb 2008ax (A. Pastorello et al. 2008) and 2011dh (M. Ergon et al. 2014). These comparison objects are selected to maintain consistency with the optical comparison. SN 2007Y and SN 1993J are not included in this plot owing to the unavailability of NIR spectra, either because they were not obtained or because they are not publicly available.

Table 4
Position of the Minimum of the Absorption Component of the P Cygni Profile

Epoch[a]	MJD	Hα/Si II λ6355 (Å)	He I λ5876 (Å)	He I λ6678 (Å)	Fe II λ4561 (Å)	Fe II λ5018 (Å)	Fe II λ5169 (Å)
2.7	59629.4	6172.5	5623.7	…	…	…	…
2.9	59629.6	6183.5	5590.9	…	…	…	…
3.1	59629.8	6177.0	5638.5	…	…	…	…
4.8	59631.5	6218.0	5678.4	…	…	…	…
6.7	59633.4	6237.1	5709.2		4378.0	4814.7	4997.8
7.5	59634.2	…	…	…	4397.2	4842.4	5014.6
7.8	59634.5	6240.0	5657.1		4400.2	4843.7	5014.8
10.6	59637.3	6246.9	5725.6	6500.2	4418.3	4856.7	5020.4
11.6	59638.3	…	…	…	4419.6	4859.1	5025.3
11.6	59638.3	6252.2	…	6503.2	…	…	…
11.8	59638.5	6247.9	5730.6	6513.6	4417.4	4857.0	5029.8
14.7	59641.4	6253.6	5769.5	6516.0	4428.1	4863.0	5041.3
17.7	59644.3	6261.7	5771.3	6556.0	4436.3	4870.9	5049.0
21.0	59647.6	6271.4	5762.9	6562.6	…	…	…
21.6	59648.3	…	…	…	4438.9	4886.3	5060.6
21.6	59648.3	6279.7	5767.4	6580.3	…	…	…
22.6	59649.3	6280.6	5767.6	6568.9	…	…	…
22.6	59649.3	6290.1	5774.3	6580.0	4440.8	4878.9	5077.2
24.6	59651.3	6288.1	5760.5	6567.7	…	…	…
24.8	59651.5	6289.8	5759.7	6573.8	4438.1	4904.1	5073.3
28.6	59655.3	6303.8	5745.4	6560.9	…	4920.3	5088.0
30.6	59657.3	6320.6	5744.5	6563.6	…	4927.3	5093.5

Note.
[a] Epoch is measured from the explosion (JD 2,459,627.19).

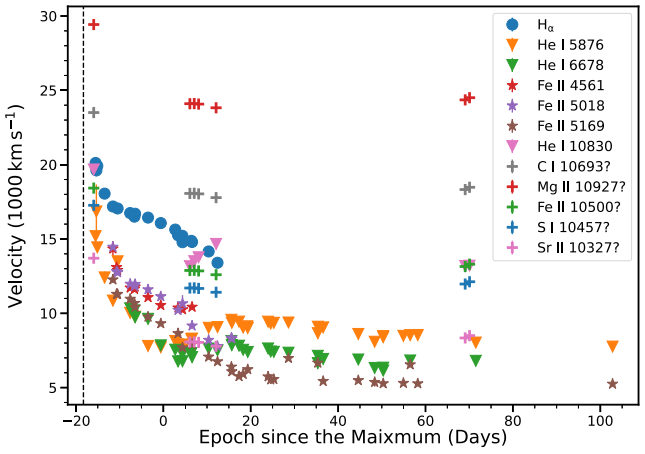

Figure 7. Velocity evolution of Hα, He I, Fe II, and feature A (see Section 5.3). The epoch of the explosion is marked with the vertical dashed line. The velocity of feature A is calculated assuming it is from C I λ1.0693 μm, Mg I λ1.0927 μm, Fe II λ1.05 μm, S I λ1.0457 μm, and Sr I λ1.0327 μm, and is shown with the plus symbol. The velocity of Hα shows a rapid drop after the V_{max}. As discussed in Section 6.1, the 6200 Å feature is likely dominated by Si II after V_{max}, so this drop does not reliably reflect the velocity evolution of the Hα line.

In general, the NIR line evolution of SN 2022crv is consistent with that of other SNe Ib/IIb. However, at around 1.005 μm, there is an extra absorption feature on the blue side of He I λ1.083 μm, hereafter referred to as "feature A." A similar feature is likely present in SN 2008D and SN 2008ax, but it is only at late times and not as strong as the feature in SN 2022crv. To the best of our knowledge, this is the first time that such a strong feature has been observed in an SESN. In order to isolate feature A from the He I λ1.083 μm line, we fit two-Gaussian functions around this region (see the left panel of Figure 14). For the origin of feature A, we consider six possibilities: C I λ1.0693 μm, Mg I λ1.0927 μm, high-velocity He I λ1.083 μm, Fe II λ1.05 μm, S I λ1.0457 μm, and Sr II λ1.0327 μm. The velocity of feature A is indicated in Figure 14 as well as in Figure 7, assuming this line is from the C I, Mg I, Fe II, S I, and Sr II.

The derived velocities of C I λ1.0693 μm and Mg I λ1.0927 μm are higher than the velocity of Hα, so these two lines can be ruled out unless there is C and Mg present at a higher velocity than the H envelope. In addition, since there is no clear evidence of any blue component around He I λ20,581 (see the right panel of Figure 14), it is unlikely this extra absorption line is from high-velocity He I λ1.083 μm.

S I λ1.0457 μm, Fe II λ1.05 μm, and Sr II λ1.0327 μm give reasonable velocities. However, S I λ1.0457 μm is usually seen in He-poor SNe (J. Teffs et al. 2020; M. Shahbandeh et al. 2022), so it is unclear if such strong S I λ1.0457 μm can be present in a He-strong SN. We could not identify other lines from S I in the NIR spectra, probably because other S I lines are rather weak. The Fe II λ1.05 μm line is commonly seen in SNe Ia but not in CCSNe. If feature A is from Fe II λ1.05 μm, the derived velocity is lower than the velocity of Hα but larger than those of He and Fe lines in the optical, indicating that this line is formed in the outer layers of the ejecta. For SESNe, some degree of mixing is required to explain the observed properties (T. Shigeyama et al. 1990; S. E. Woosley & R. G. Eastman 1997; L. Dessart et al. 2012; S.-C. Yoon et al. 2019), so it is possible that the Fe II λ1.05 μm line is formed by material mixed into the outer layer. In addition, the ejecta of SESNe may be aspherical (e.g., S. Taubenberger et al. 2009; D. Milisavljevic et al. 2010; Q. Fang et al. 2022). In this case, Fe II λ1.05 μm lines would be formed at higher velocities. However, no other Fe II lines are identified in the NIR spectra, making this possibility less realistic. If feature A is from Sr II λ1.0327 μm, its velocity could be similar to the velocity of

Table 5
Absorption Flux Minimum of P Cygni Profile

Epoch[a]	MJD	He I λ5876 (Å)	He I λ6678 (Å)	Fe II λ5018 (Å)	Fe II λ5169 (Å)
33.8	59660.5	5734.7	6549.4	4917.8	5099.7
33.9	59660.6	5738.8	6555.8	4918.7	5105.2
35.6	59662.2	5737.2	6556.6	⋯	5110.8
37.5	59664.2	5743.4	⋯	⋯	⋯
36.5	59663.2	5745.1	6562.7	⋯	⋯
36.5	59663.2	⋯	⋯	⋯	5108.1
37.6	59664.2	5745.6	6566.0	⋯	5102.7
42.2	59668.9	5737.3	6560.8	⋯	5111.2
42.8	59669.5	5739.7	6565.4	⋯	5114.7
43.5	59670.2	5738.8	6565.8	⋯	5114.1
46.9	59673.6	5738.4	6567.1	⋯	5089.6
53.6	59680.3	5743.9	6571.8	⋯	5095.0
53.6	59680.3	5752.6	6582.9	⋯	⋯
54.8	59681.5	5744.9	6576.5	⋯	5116.4
62.9	59689.5	5753.6	6577.4	⋯	5115.5
66.6	59693.3	5763.9	6590.2	⋯	5117.6
68.6	59695.2	⋯	⋯	⋯	5119.2
68.6	59695.2	5757.8	6589.7	⋯	⋯
68.6	59695.2	5756.4	6594.2	⋯	⋯
73.2	59699.9	5756.1	⋯	⋯	5118.7
74.7	59701.4	5755.1	6578.9	⋯	5097.0
76.5	59703.2	⋯	⋯	⋯	5119.2
76.5	59703.2	5755.0	⋯	⋯	⋯
89.7	59716.4	5765.0	6579.4	⋯	⋯
121.0	59747.7	5770.3	⋯	⋯	5119.7

Note.
[a] Epoch is measured from the explosion date (JD 2,459,627.19).

Fe lines in optical. Sr II λ1.0327 μm is common in SNe II (S. Davis et al. 2019), so it is possible this line can be seen in an SESN given that they are all core collapses of massive stars. A possible absorption line from Sr II λ1.0036 μm at the same velocity (∼8000 km s^{-1}) is likely present in the NIR spectra, which is marked using a gray dashed line in Figure 14. This makes Sr II λ1.0327 μm the most plausible explanation of feature A.

In conclusion, feature A observed in SN 2022crv is likely due to Sr II λ1.0327 μm, but we could not fully exclude Fe II λ1.05 μm and S I λ1.0457 μm. Further detailed hydrodynamic modeling is needed to investigate the origin of feature A.

6. Discussion

6.1. Classification

Although there are clear definitions for each subtype of SESN, the actual classification for individual objects can be nontrivial. This is because the classification for some SESNe can be time dependent (e.g., D. Milisavljevic et al. 2013; G. Folatelli et al. 2014; M. Modjaz et al. 2019; M. Williamson et al. 2019; S. Holmbo et al. 2023). In addition, there is likely a continuum between the subtypes (although see S. Holmbo et al. 2023). For instance, it has been suggested there is likely a gradual transition from SNe IIb to SNe Ib depending on the amount of residual hydrogen in the envelope (e.g., S. J. Prentice & P. A. Mazzali 2017). Furthermore, hydrogen has been suspected to be present in many SNe Ib, suggesting that these objects may still maintain low-mass hydrogen envelopes (e.g., J. S. Deng et al. 2000; D. Branch et al. 2002; A. Elmhamdi et al. 2006; J. Parrent et al. 2007; S. James & E. Baron 2010). This makes the distinction between SNe Ib and SNe IIb more vague.

In recent years, many efforts have been made to improve the classification system of SESNe (Y.-Q. Liu et al. 2016; S. J. Prentice & P. A. Mazzali 2017; M. Williamson et al. 2019; S. Holmbo et al. 2023). In this section, we will apply the classification methods proposed by Y.-Q. Liu et al. (2016); S. J. Prentice & P. A. Mazzali (2017), and M. Williamson et al. (2019) to SN 2022crv. In the studies of Y.-Q. Liu et al. (2016) and S. J. Prentice & P. A. Mazzali (2017), the absorption line at ∼6200 Å observed in both SNe Ib and SNe IIb is attributed to Hα, with the primary differences being the evolution and strength of the Hα line. We will discuss the classification of SN 2022crv and demonstrate that this object appears to be an outlier in some of the classification schemes mentioned above. It is important to note that the discussion of whether the ∼6200 Å line in SNe Ib is truly due to Hα is beyond the scope of this paper.

SN 2022crv was initially classified as an SN Ib (J. E. Andrews et al. 2022). However, as we discussed in Section 5, a strong absorption line is visible around 6200 Å during early phases and could be related to Hα. Shortly after maximum brightness, this line disappears and the spectral evolution of SN 2022crv is almost identical to that of other SNe Ib. Such evolution makes SN 2022crv more like an SN IIb. A small notch around 4595 Å is observed in the early phases of SN 2022crv (see Figure 6) and could be due to Hβ. To get a better sense of where SN 2022crv stands among SESNe, in Figure 15, we compare the observed spectra with the mean spectral templates of SNe IIb, Ib, and Ic from Y.-Q. Liu et al. (2016). The observed spectra shown here have been flattened

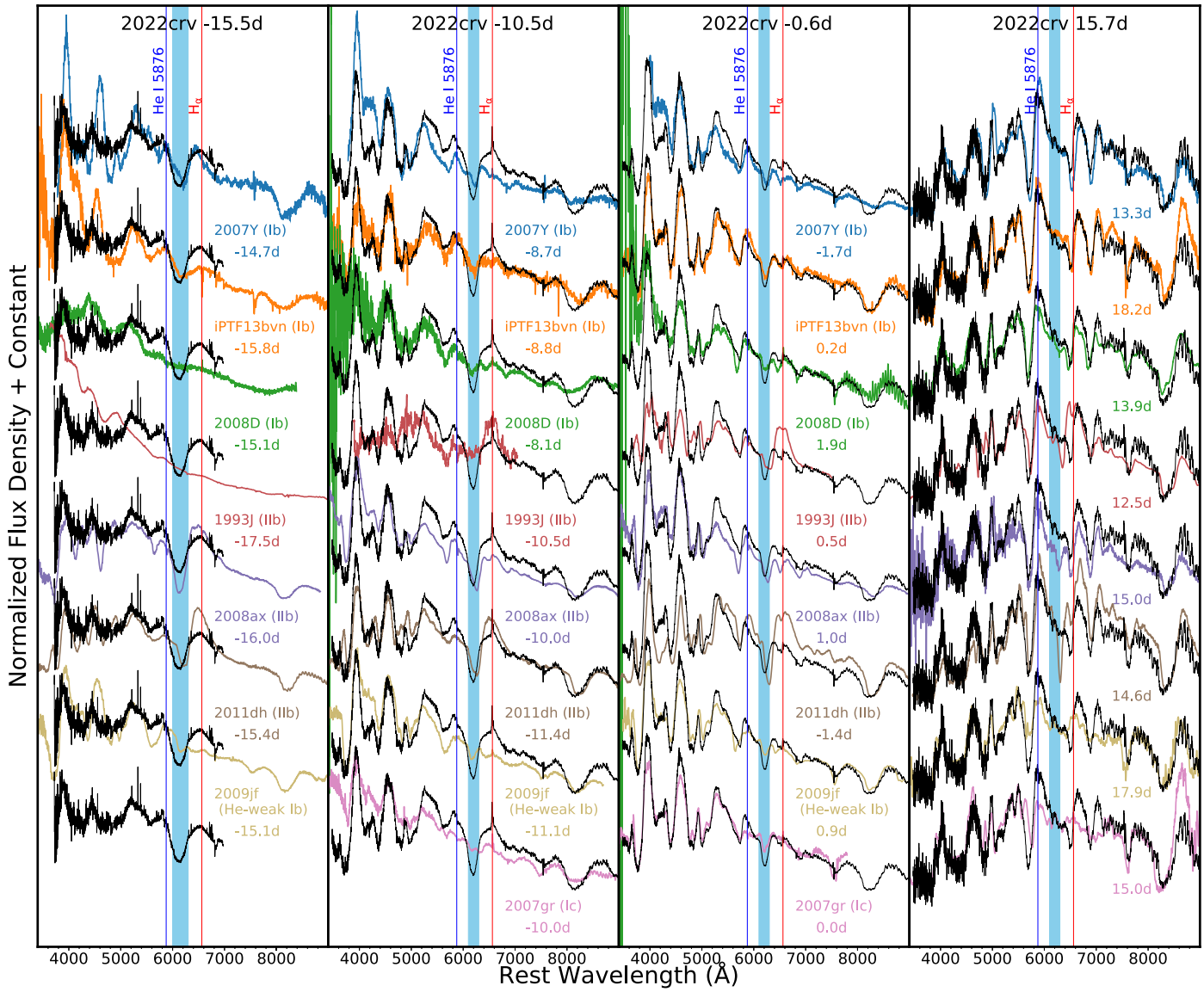

Figure 8. Optical spectral comparison of SN 2022crv to other well-studied SESNe, including SNe Ib (SN 2007Y, iPTF13bvn, SN 2008D), SNe IIb (SN 1993J, SN 2008ax, SN 2011dh, SN 2009jf), and SNe Ic (SN 2007gr). The blue shaded areas mark the 6200 Å feature.

using SNID following the procedure outlined by S. Blondin & J. L. Tonry (2007). At about days −10 and 0, the 6200 Å absorption line in SN 2022crv is as strong as that in the mean spectra of SNe IIb. The 6200 Å absorption line in SN 2022crv exhibits a higher velocity compared to that in the mean spectra of SNe IIb, and is similar to that in the mean spectra of SNe Ib. At about day 15, the spectrum of SN 2022crv is almost identical to the mean spectra of SNe Ib, while the mean spectra of SNe IIb still display a strong 6200 Å absorption line.

If the 6200 Å line is indeed attributed to Hα, SN 2022crv should be classified as an SN IIb. However, the high velocity and the rapid disappearance of Hα complicate the classification. Y.-Q. Liu et al. (2016) found that the 6200 Å line velocities in SNe Ib are systematically larger than in SNe IIb (assuming the 6200 Å line in SNe Ib is due to Hα), and the pseudo-equivalent width (pEW) values of the 6200 Å line in SNe Ib are smaller than in SNe IIb, consistent with the consensus that SNe IIb have more hydrogen in their envelopes. They thus proposed that the pEW can be used to differentiate between SNe Ib and SNe IIb at all epochs. That being said, if an object is classified as an SNe Ib/IIb using the 6200 Å line pEW, the classification will not change over time since SNe IIb always maintain a larger 6200 Å line pEW. This result has been further supported by S. Holmbo et al. (2023) based on the spectroscopic analysis of a large sample of SESNe.

In Figure 16, we compare the velocity and pEW evolution of the 6200 Å absorption line in SN 2022crv, assuming it is from Hα with those of objects presented by Y.-Q. Liu et al. (2016). SN 2022crv shows a high pEW at early phases similar to other SNe IIb, followed by a rapid decline, and has a similar pEW value to other SNe Ib about 10 days after *V*-band maximum brightness. The velocity of the 6200 Å line in SN 2022crv is generally higher than in SNe IIb and is more similar to that in SNe Ib. This pEW transition from SNe IIb to SNe Ib seems to be an outlier in the classification scheme using the pEW of the 6200 Å line proposed by Y.-Q. Liu et al. (2016).

To quantitatively illustrate the complications involved in this classification, we applied the principal component and SVM classification method described by M. Williamson et al. (2019).

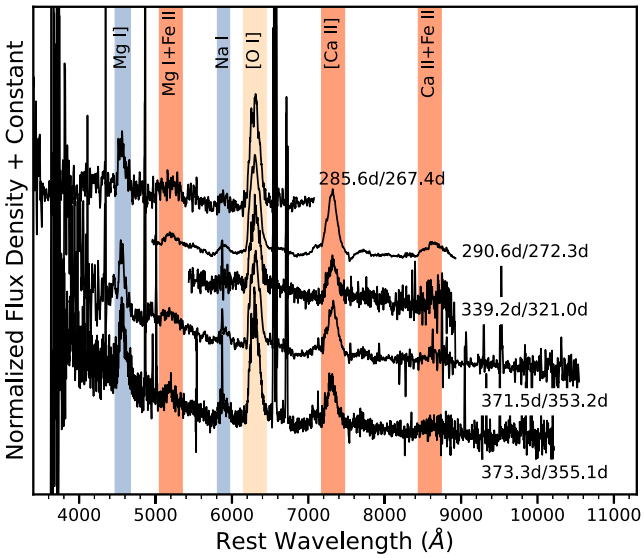

Figure 9. The nebular phase spectroscopic evolution of SN 2022crv. Phase is measured from the dates of the explosion and *V*-band maximum brightness. All spectra shown here are rebinned with a second-order Savitzky–Golay filter with a window size of 11 Å. These spectra are available in machine readable format at the data behind the figure.

(The data used to create this figure are available in the online article.)

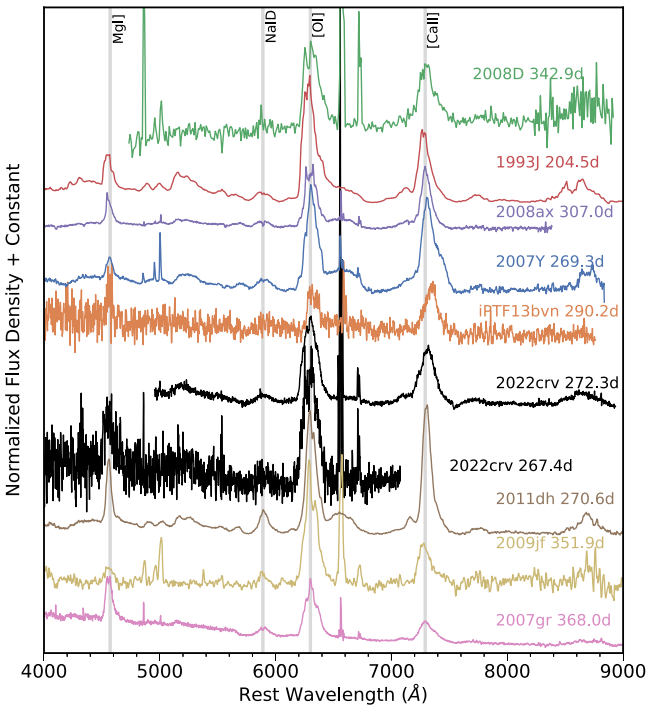

Figure 10. Nebular spectra of SN 2022crv compared with those of other SESNe. The phase is measured from the date of the *V*-band maximum brightness.

The code has been updated to allow a time-dependent classification of SESNe (M. Williamson & M. Modjaz 2024, in preparation). The result is shown in Figure 17. Initially, SN 2022crv is located in the SN Ic-BL (broad-line) region. This is likely due to the spectrum at day −15.1 dominated by the strong high-velocity Hα, which can be misidentified as the broad Si II λ6355 line in SNe Ic-BL. At roughly day −13 to day −10, SN 2022crv is more similar to SNe IIb. After around day −10, it is more consistent with SNe Ib.

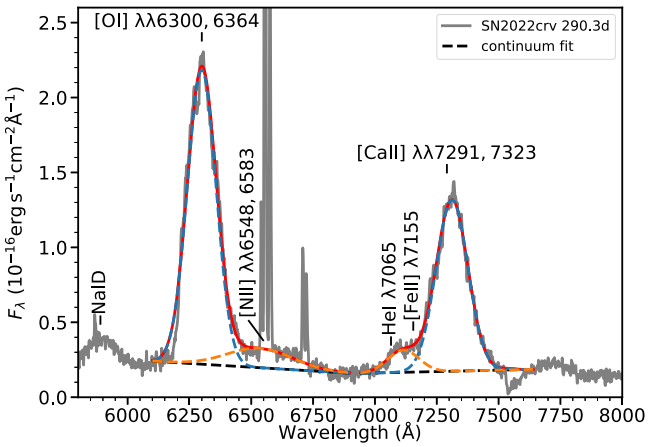

Figure 11. Line identification of the nebular spectrum taken on day 272.3 (290.6 days after the explosion). A double Gaussian function is fitted around each of 6300 Å and 7300 Å, to respectively deblend [O I] and [Ca II] from other lines. The continuum is defined by a straight segment connecting the two local minima.

S. J. Prentice & P. A. Mazzali (2017) proposed to use the strength and ratio between absorption and emission of Hα to classify He-rich SNe. They suggested that He-rich SESNe can be split into four groups [IIb, IIb(I), Ib(II), and Ib] from hydrogen-rich to hydrogen-poor. Following the method described by S. J. Prentice & P. A. Mazzali (2017), the ratio between absorption and emission of Hα in SN 2022crv before peak brightness is measured to be ∼0.3, and the average EW before maximum brightness is about 73 Å. These values make SN 2022crv marginally fall into the IIb(I) category. The ratio between absorption and emission of Hα is a good probe of the extent of the hydrogen envelope, and a larger ratio indicates a more extended hydrogen envelope (S. J. Prentice & P. A. Mazzali 2017). A classification of IIb(I) implies that the amount of hydrogen in SN 2022crv is larger than in normal SNe Ib but smaller than in SNe IIb, suggesting that SN 2022crv is an intermediate object between these two classes.

In summary, the 6200 Å line velocity evolution of SN 2022crv is consistent with that of SNe Ib; the 6200 Å line pEW evolution of SN 2022crv gradually transitions from SNe IIb to SNe Ib, a behavior not observed in the sample studied by Y.-Q. Liu et al. (2016). The amount of hydrogen in SN 2022crv is likely between that in SNe Ib and SNe IIb, suggesting SN 2022crv is a representative transitional object on the proposed continuum between SNe IIb and SNe Ib.

6.2. Hydrogen Envelope

Quantifying how much hydrogen is still present in the progenitor right before the explosion is important for understanding the mass-loss history and thus the progenitor system. In this section, we will use both a semianalytic method and hydrodynamic modeling to constrain the mass of hydrogen retained in the progenitor right before the explosion.

The velocity of Hα in SN 2022crv is generally higher than that of SNe IIb. The higher velocity of Hα could be a result of larger explosion energy or smaller hydrogen mass. Assuming that the He I line appears when the surrounding hydrogen envelope becomes optically thin and the SN expansion is homologous, G. H. Marion et al. (2014) proposed a method to roughly estimate the mass of the hydrogen envelope: $M_{\rm H} \propto (v_{\rm H}\, t_{\rm He})^2$, where $v_{\rm H}$ is the velocity of the outer edge of

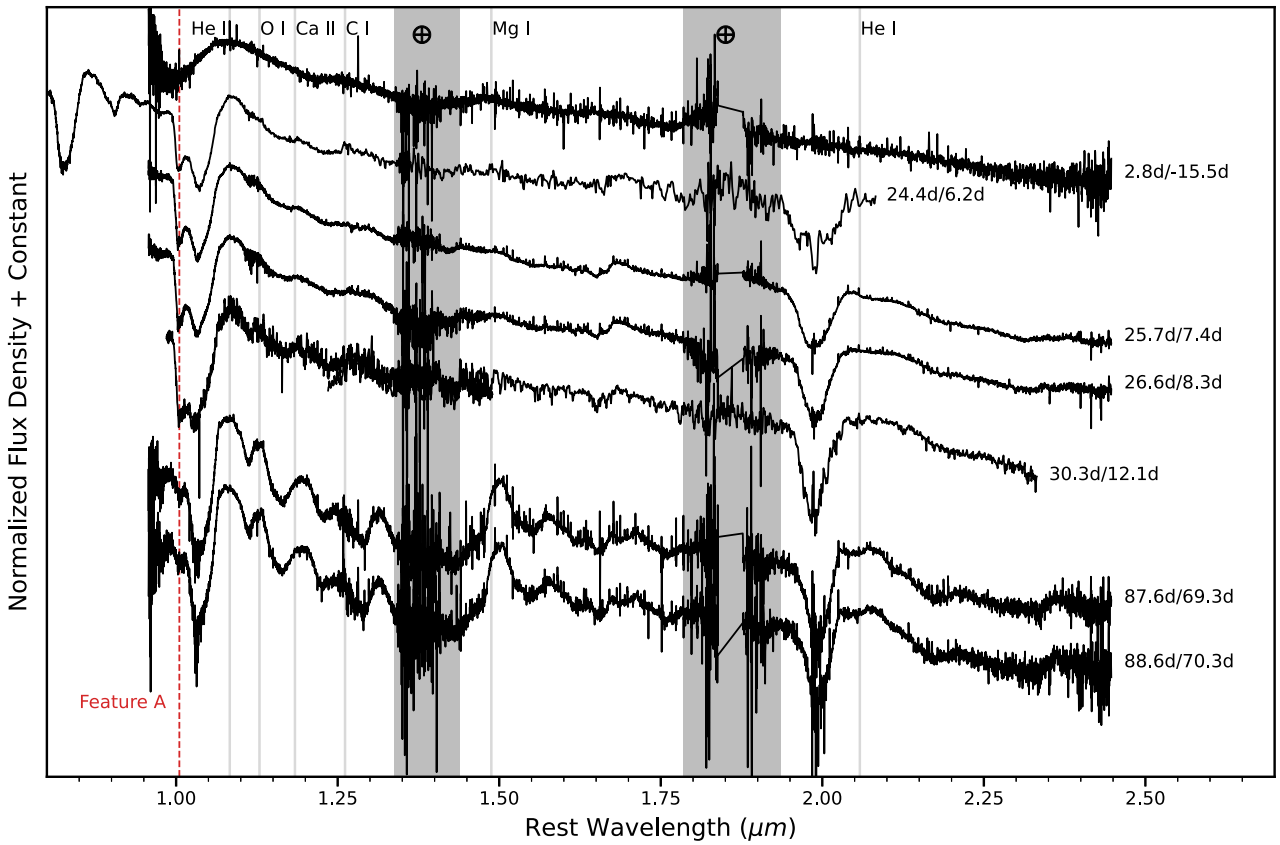

Figure 12. NIR spectra of SN 2022crv. The phase is measured from the dates of explosion and *V*-band maximum brightness. The red dashed line marks the extra absorption feature on the blue side of He I λ1.083 μm. The high telluric absorption regions are marked with gray bands. These spectra are available in machine readable format at the data behind the figure.

(The data used to create this figure are available in the online article.)

the hydrogen envelope and $t_{\rm He}$ is the time when the He line is first observed, and the constant of proportionality is empirically calculated by scaling to a reference SN. For SN 2022crv, $v_{\rm H}$ is about 30,000 km s^{-1}. The He line in SN 2022crv can be clearly seen in the first spectrum, so we can limit $t_{\rm He} < 2.7$ days. Using SN 1993J and SN 2011dh as references, we find $M_{\rm H}(2022{\rm crv}) < 0.14\,M_{\rm H}(2011{\rm dh})$ and $M_{\rm H}(2022{\rm crv}) < 0.05\,M_{\rm H}(1993{\rm J})$. For SN 2011dh and SN 1993J, a recent study by A. Gilkis & I. Arcavi (2022) estimated hydrogen masses of $\sim$0.035 $M_\odot$ and $\sim$0.1 $M_\odot$, respectively. Therefore, the hydrogen envelope mass in SN 2022crv can be constrained to be $M_{\rm H}(2022{\rm crv}) < 5 \times 10^{-3}$ $M_\odot$. This small hydrogen mass is consistent with the higher velocity and the quick disappearance of the Hα in SN 2022crv. However, this seems to contradict the large pEW at early phases.

In order to investigate if a small hydrogen envelope can produce the evolution of the Hα line in SN 2022crv, we compare the observed spectra of SN 2022crv with the SESN models of L. Dessart et al. (2015, 2016) (3p65Ax2 and 3p0Ax1) and S. E. Woosley et al. (2021) (He3.40 and He5.38); see Figure 18. The He3.40 and the He5.38 spectra are produced based on models presented by S. E. Woosley (2019) and T. Ertl et al. (2020), and they do not include any hydrogen. The 3p65Ax2 and the 3p0Ax1 spectra are based on models presented by S. C. Yoon et al. (2010), with hydrogen masses of 4.72×10^{-3} $M_\odot$ and 7.92×10^{-4} $M_\odot$, respectively.

Both the 3p65Ax2 and 3p0Ax1 models nicely reproduce the early-time broad absorption line at 6200 Å and other main features in the observed spectra (Figure 18), while the 3p0Ax1 model gives a better fit. The 6200 Å feature in these two models has been attributed to Hα at early phases and Si II before maximum light (L. Dessart et al. 2015). This is also likely what happened in SN 2022crv. At early times, the broad absorption line at 6200 Å is mainly from hydrogen, but as the object evolves, the 6200 Å feature becomes narrower and more dominated by Si II. The 6200 Å feature is missing in the hydrogen-free He3.40 and He5.38 models at 2.7 days. At 17.7 days after the explosion, these models show weak absorption lines around 6200 Å, which are identified as Si II by S. E. Woosley et al. (2021). We note that the models we use here are not specifically made for SN 2022crv, so the hydrogen mass we derive can be treated only as an order of magnitude estimate. For example, the models from L. Dessart et al. (2016) have peak luminosities fainter than that of SN 2022crv, possibly due to a lower explosion energy or lower nickel mass synthesized in the model. Detailed modeling would be required in future studies to better constrain the mass of hydrogen left in the progenitor envelope of SN 2022crv.

The early light curve of SN 2022crv does not show signs of cooling envelope emission, and the nebular spectra also lack hydrogen emission, consistent with the compact progenitor scenario proposed by R. A. Chevalier & A. M. Soderberg (2010). Therefore, SN 2022crv likely has a compact progenitor with an extremely small amount of hydrogen.

In conclusion, the hydrogen envelope in SN 2022crv is likely on the order of 10^{-3} $M_\odot$. From the model comparison, we found that the 6200 Å line is likely a mixture of Hα and Si II. At early phases

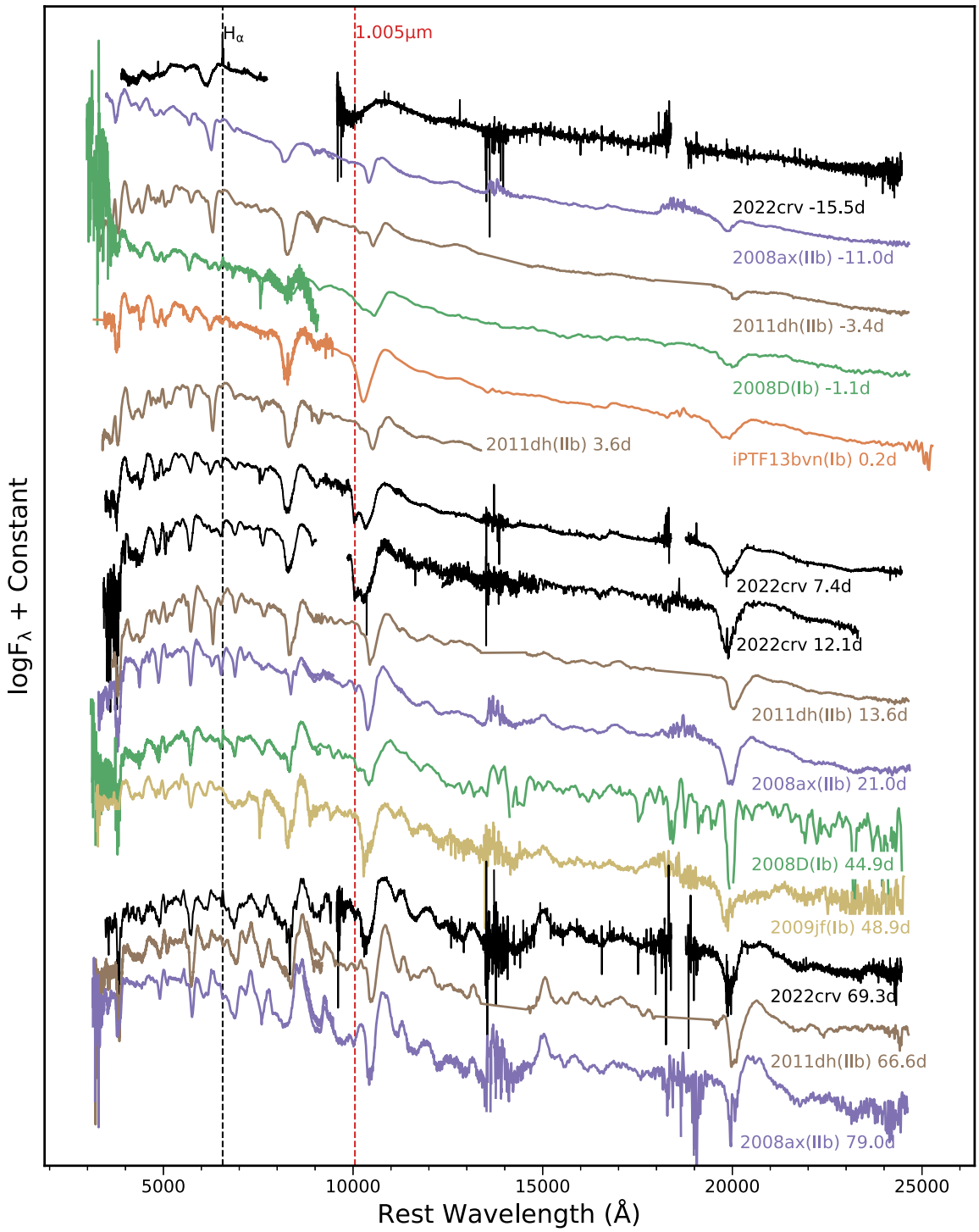

Figure 13. Comparison of combined optical and NIR spectra of SN 2022crv with those of other SNe Ib/IIb. The positions of Hα (black dashed line) and 1.005 μm (red dashed line) are marked.

(within 15 days after the explosion), the 6200 Å line is likely dominated by hydrogen; thereafter, it is likely mainly due to Si II.

6.3. Explosion Properties

6.3.1. Explosion Geometry

At late times, when the SN ejecta become optically thin, spectra can provide useful information about the inner structure of the SN. For SESNe, the line profile of [O I] $\lambda\lambda$ 6300, 6364 is often used to study the geometry of the explosion (P. A. Mazzali et al. 2005; K. Maeda et al. 2008; M. Modjaz et al. 2008; S. Taubenberger et al. 2009; D. Milisavljevic et al. 2010; Q. Fang et al. 2022). The [O I] line in SN 2022crv shows an asymmetric profile (see Figure 19), with a prominent peak at around 6300 Å and a blueshifted peak around 6270 Å (-1430 km s^{-1}). The separation of the two peaks is 30 Å smaller than the separation of the [O I] $\lambda\lambda$ 6300, 6364 doublet. An asymmetric profile could originate from the oxygen-rich

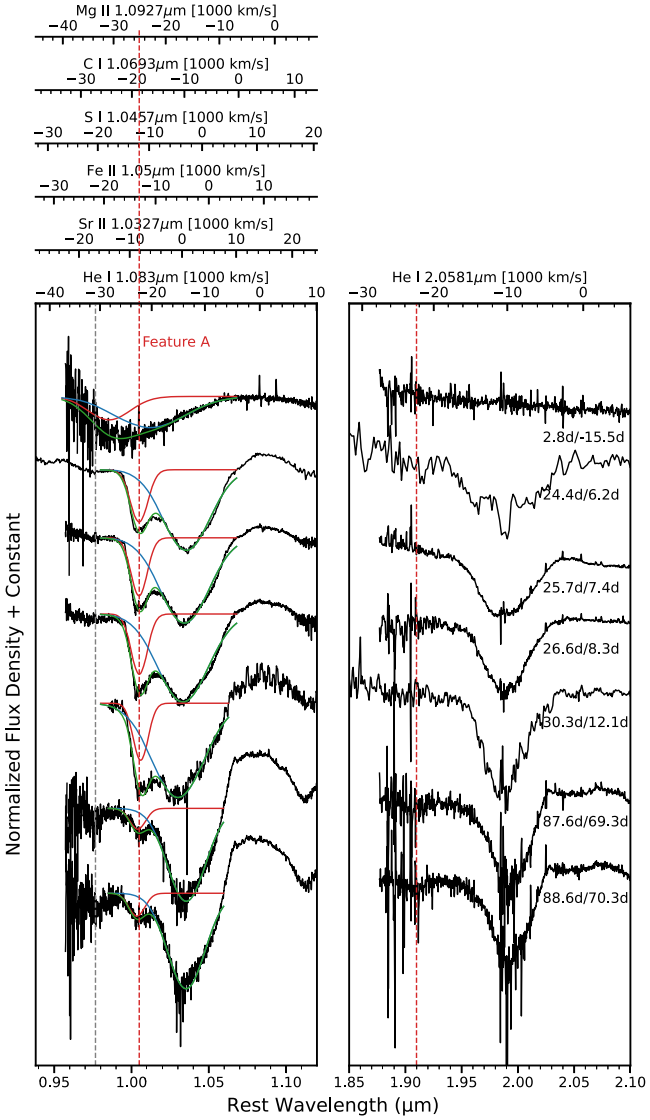

Figure 14. Spectral evolution of SN 2022crv in the 1 and 2 μm regions. The phase is measured from the dates of explosion and *V*-band maximum light. Feature A can be fit with a two-Gaussian function. The velocity scales of C I λ1.0693 μm, Mg I λ1.0927 μm, high-velocity He I λ1.083 μm, Fe II λ1.05 μm, S I λ1.0457 μm, and Sr II λ1.0327 μm are shown in the top abscissa axis. In the left panel, the red dashed line roughly marks the position of feature A at 1.005 μm, corresponding to $\sim$23,280 km s^{-1}, assuming feature A is from He I λ1.083 μm. The red dashed line in the right panel also has a velocity of $\sim$23,280 km s^{-1} with respect to He I λ20,581. The gray dashed line marks the possible identification of Sr II λ1.0036 μm, at a velocity of $\sim$8000 km s^{-1}.

material with a torus-like structure (P. A. Mazzali et al. 2005; K. Maeda et al. 2008; S. Valenti et al. 2008). However, in this model, the [O I] line would display either a double-peaked profile if viewed from a direction close to the plane of the torus or a single-peaked profile if viewed from a direction perpendicular to the torus. Such a scenario is hard to explain in the case of SN 2022crv owing to the lack of a redshifted emission line. If this asymmetric profile is indeed from a torus-like structure, then the emission from the rear side is likely scattered by the ejecta or absorbed by dust (D. Milisavljevic et al. 2010). For SN 2022crv, a clear sign of CO formation is detected about 100 days after the explosion (J. Rho et al. 2024, in preparation), implying that dust could form at sufficiently late phases.

I. Maurer et al. (2010) suggested that the double-peaked profile observed in the [O I] line can be caused by the high-velocity Hα absorption. Given that a high-velocity feature is detected at early phases in SN 2022crv, this scenario cannot be ruled out. If the trough around 6285 Å is due to Hα absorption, the corresponding velocity would be $\sim$12,700 km s^{-1}. There is no clear evidence of Hβ found in the nebular spectra of SN 2022crv, likely owing to the low signal-to-noise ratio of the blue portion of the spectra. If Hα is responsible for the asymmetric profile of the [O I] line, the ejecta of SN 2022crv would be almost spherically symmetric.

6.3.2. Oxygen Mass and Progenitor Mass

Theoretical studies have shown that the initial progenitor mass of an SN strongly correlates with the oxygen mass in the SN ejecta (S. E. Woosley & T. A. Weaver 1995; A. Jerkstrand et al. 2015; L. Dessart et al. 2021, 2023). The flux of the [O I] $\lambda\lambda$ 6300, 6364 emission line during the nebular phase has been demonstrated to be a powerful diagnostic tool to constrain the oxygen mass (A. Uomoto 1986; A. Jerkstrand et al. 2012; L. Dessart et al. 2021). In addition, the line ratio of [O I] $\lambda\lambda$ 6300, 6364/[Ca II] $\lambda\lambda$ 7291, 7323 can be an indicator of the progenitor mass of an SESN, since synthesized Ca is not sensitive to the main-sequence mass of the progenitor (K. Nomoto et al. 2006).

A. Uomoto (1986) showed that the minimal oxygen mass in the SN ejecta can be calculated as

$$\frac{M_{\rm oxygen}}{M_\odot} = 10^8\,(D/{\rm Mpc})^2\,F([{\rm O\,I}])\exp(22,\,80\ {\rm K}\ T^{-1}), \quad (1)$$

where D is the distance of the SN in megaparsec, F([O I]) is the flux of the [O I] line in erg per second per square cm, and T is the temperature of the oxygen-emitting gas in Kelvin. T can be estimated by using the [O I] λ5577/[O I] $\lambda\lambda$ 6300, 6364 flux ratio (J. C. Houck & C. Fransson 1996; A. Elmhamdi et al. 2004). This method is only valid when the gas density is low and the [O I] lines are formed mainly by collisional excitation. However, the [O I] λ5577 line in SN 2022crv is not clearly detected, indicating a low temperature. [O I] λ5577 was also not detected in SN 1990I, and A. Elmhamdi et al. (2004) put a lower limit on the [O I] λ5577/[O I] $\lambda\lambda$ 6300, 6364 flux ratio by using a temperature of 3200–3500 K for the line-emitting region of SN 1990I. D. K. Sahu et al. (2011) used a temperature of 4000 K for SN 2009jf since the [O I] λ5577 line was not visible in its nebular spectra. For SN 2022crv, we assume the temperature of the line-emitting region is $\sim$3200–4000 K, which results in an oxygen mass of $\sim$0.9–3.5 $M_\odot$.

In Section 5.2, the [O I]/[Ca II] ratio in SN 2022crv is measured to be $\sim$1.5. H. Kuncarayakti et al. (2015) measured the [O I]/[Ca II] ratio in a group of CCSNe, and they found that there is a natural spread among SNe Ib/c. This observed spread is likely an indication of two progenitor populations of SESNe: a single massive Wolf–Rayet star and a low-mass star in a binary system (H. Kuncarayakti et al. 2015). An [O I]/[Ca II] ratio of 1.5 indicates that the progenitor of SN 2022crv is more likely a less massive star. At solar metallicity, the minimum zero-age main-sequence (ZAMS) mass ($M_{\rm ZAMS}$) for a single star to lose its hydrogen envelope via stellar winds and become a Wolf–Rayet star is about 25–35 $M_\odot$ (P. A. Crowther 2007; T. Sukhbold et al. 2016; T. Ertl et al. 2020). As we discussed in

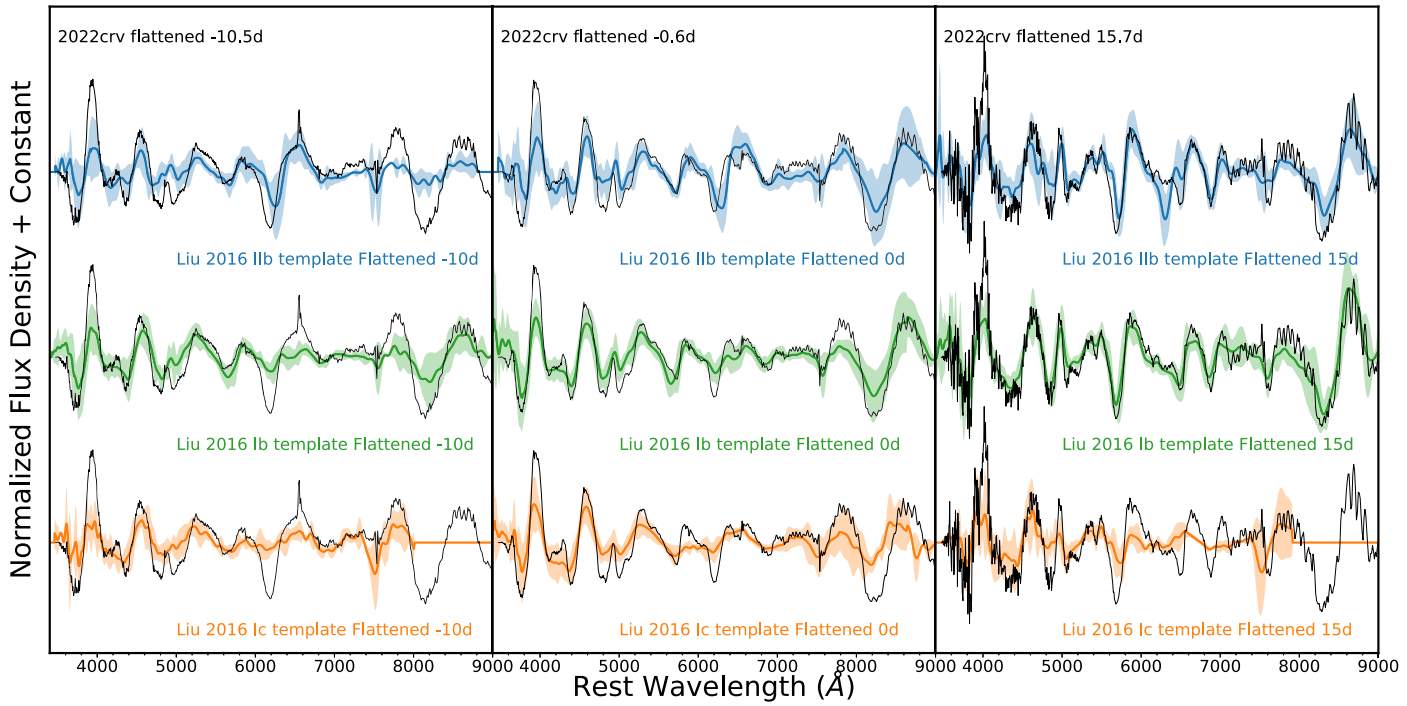

Figure 15. Observed spectra of SN 2022crv compared with the mean spectra (the solid lines) and the standard deviations (the shaded regions) of SNe IIb, Ib, and Ic from Y.-Q. Liu et al. (2016). The observed spectra have been flattened using SNID.

Section 3.4, the metallicity at the location of SN 2022crv is only slightly larger than solar metallicity. This implies that the progenitor was likely in a binary system with $M_{\rm ZAMS}$ less than about 25–35 $M_{\odot}$, and at least a part of the hydrogen envelope was stripped during the binary interaction.

6.3.3. Progenitor Mass from Nebular Spectral Modeling

To further constrain the progenitor properties of SN 2022crv, we compare the observed spectrum with theoretical models from A. Jerkstrand et al. (2015), L. Dessart et al. (2021), and L. Dessart et al. (2023). A. Jerkstrand et al. (2015) took the single-star SN II models from S. E. Woosley & A. Heger (2007) and artificially removed most of the hydrogen envelope, and then produced spectra for SNe IIb. L. Dessart et al. (2021, 2023) modeled nebular spectra of SNe Ib/c based on models from S. E. Woosley (2019) and T. Ertl et al. (2020), which also include the effects of wind loss from the He star after the H envelope is fully stripped via the binary interaction. L. Dessart et al. (2023) found that the spectral features of SESNe are mainly dependent on their presupernova masses ($M_{\rm preSN}$) and the oxygen yields, so these models can provide constraints on the oxygen mass and $M_{\rm preSN}$ of SN 2022crv.

The nebular spectra of SN 2022crv at days 290.6 and 371.5 are likely contaminated by the host-galaxy background. Therefore, we fit the observed spectrum with a linear combination of the SN spectrum and a star-forming galaxy template spectrum from A. L. Kinney et al. (1996) as the first-order approximation of the host background. As the SN fades, this contamination becomes more dominant and harder to remove from the SN spectrum. At day 371.5, the object is highly contaminated by the host background below ∼5800 Å. However, we note that this contamination does not affect our estimation of the progenitor properties since we are only interested in the region redward of ∼6000 Å. The comparisons are shown in Figures 20 and 21, while the physical properties of these models are summarized in Table 6.

For the models from L. Dessart et al. (2021, 2023), we found that the [O I] intensity of SN 2022crv is between those of the He6.0 and He8.0 models. Other features of the observed spectrum, such as Na I $\lambda\lambda$ 5896, 5890, [N II] $\lambda\lambda$ 6548,6583, and [Ca II] $\lambda\lambda$ 7291, 7323, can also be reproduced by these two models. This indicates that the mass of oxygen in SN 2022crv is 1.0–1.7 $M_{\odot}$, and $M_{\rm preSN}$ is 4.5–5.6 $M_{\odot}$. For the models from A. Jerkstrand et al. (2015), we found that the best-fit models are m13G and m17A, while [N II] $\lambda\lambda$ 6548, 6583 is stronger in model m13G than in the observed spectrum. This suggests that the oxygen mass produced in SN 2022crv is 0.5–1.3 $M_{\odot}$, and $M_{\rm preSN}$ is 3.5–5 $M_{\odot}$.

The oxygen mass and $M_{\rm preSN}$ derived from the models of L. Dessart et al. (2021, 2023) are consistent with those derived from the models of A. Jerkstrand et al. (2015), and they are also consistent with the oxygen mass we estimated using the flux of [O I] emission. Since the models in S. E. Woosley (2019) used by L. Dessart et al. (2021, 2023) employed a more updated progenitor evolution treatment than the models of S. E. Woosley & A. Heger (2007) used by A. Jerkstrand et al. (2015), we will adopt an oxygen mass of 1.0–1.7 $M_{\odot}$ and an $M_{\rm preSN}$ of 4.5–5.6 $M_{\odot}$ derived from models of L. Dessart et al. (2021, 2023).

The value of $M_{\rm ZAMS}$ of the progenitor depends on the mass-loss history of the progenitor star. Since the progenitor of SN 2022crv only retained a tiny amount of hydrogen before the explosion, $M_{\rm preSN}$ is roughly equivalent to its He-core mass. We can put constraints on $M_{\rm ZAMS}$ by considering two extreme mass-loss histories: (1) the whole hydrogen envelope of the progenitor is removed only right before the explosion, similar to the treatment by A. Jerkstrand et al. (2015); (2) the whole hydrogen envelope of the progenitor is lost close to the time of He ignition, and there is no more mass loss after that, similar to

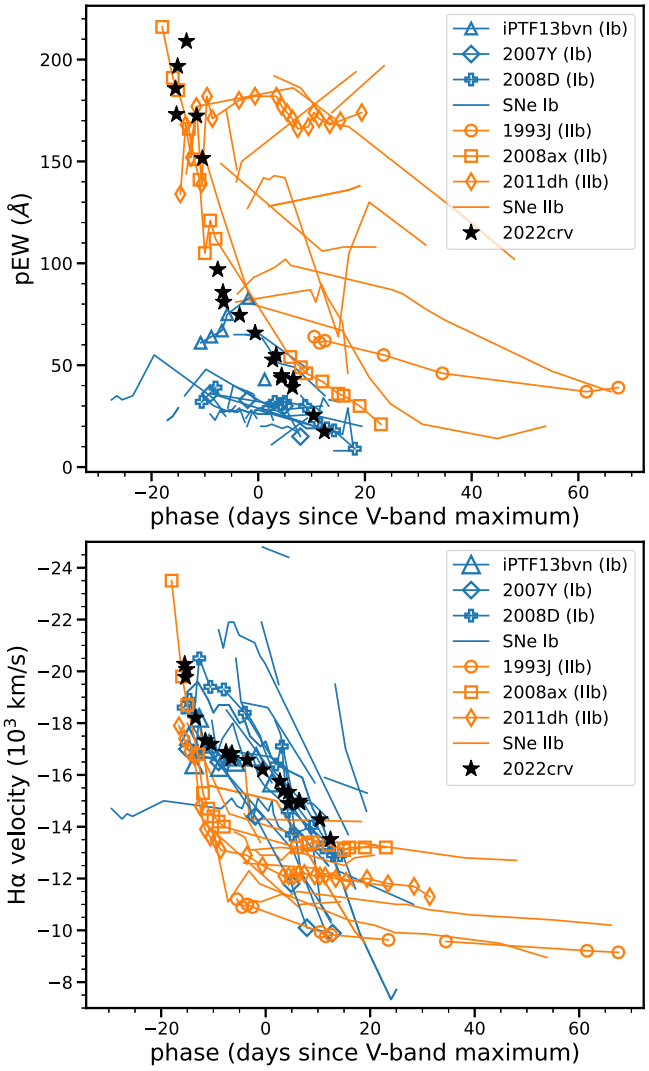

Figure 16. Upper: the pEW evolution of the 6200 Å feature of SN 2022crv compared with other SESNe. The 6200 Å feature in SN 2022crv shows a large pEW at the beginning, similar to other SNe IIb. Then, it quickly decreases until it disappears around 15 days after V_{max}. Bottom: velocity evolution of the 6200 Å feature in SN 2022crv, assuming it is from Hα. The velocity of the 6200 Å feature in SN 2022crv is generally larger than that in SNe IIb but similar to that in SNe Ib.

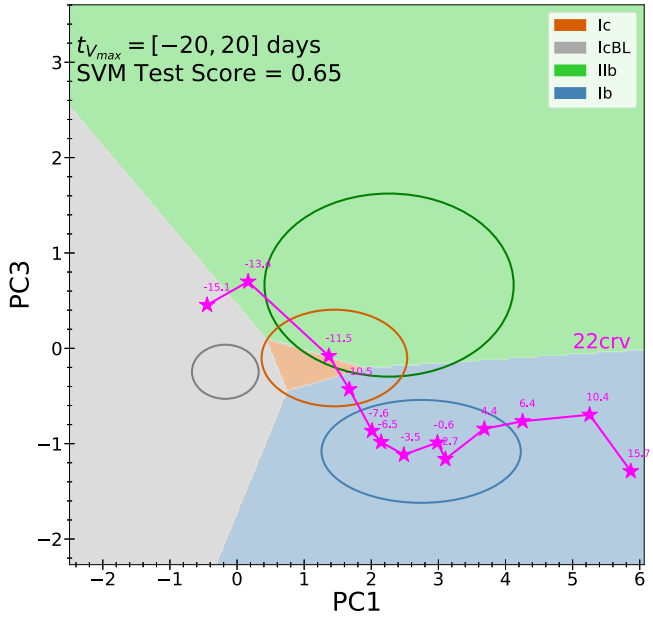

Figure 17. An SVM time-dependent spectral classification of SN 2022crv (M. Williamson & M. Modjaz 2024, in preparation) based on the methods presented by M. Williamson et al. (2019). SN 2022crv is classified as an IIb SN IIb before around −10 days from the V-band maximum brightness. After that, SN 2022crv is more similar to an SN Ib. The trajectory in principal component analysis phase space as SN 2022crv evolves (magenta) clearly shows the type of transition occurring in the spectra.

the treatment of the models without mass loss by (L. Dessart et al. 2023).

In the first case, the He-core mass would continue to grow until the explosion. To achieve the same He-core mass, the progenitor in this scenario would require a smaller $M_{\rm ZAMS}$ than the progenitor of SN 2022crv. From T. Sukhbold et al. (2016), we find that a massive star that finally has a He-core mass of 4.5–5.6 $M_\odot$ would have a $M_{\rm ZAMS}$ of ∼16–19 $M_\odot$. In the second case, the He-core mass stops growing close to the time of He-core ignition. To produce the same He-core mass, $M_{\rm ZAMS}$ in this scenario would be larger than that of SN 2022crv's progenitor. Based on Equation (4) of S. E. Woosley (2019), we find that a massive star that has a He-core mass of 4.5–5.6 $M_\odot$ at He ignition would have a $M_{\rm ZAMS}$ of ∼20–22 $M_\odot$. Therefore, $M_{\rm ZAMS}$ of the progenitor of SN 2022crv can be roughly constrained to be ∼16–22 $M_\odot$. However, we note that it is possible that the mass-loss rate prescriptions in the stellar evolution models of T. Sukhbold et al. (2016) could be too high compared to those observed in red supergiants (E. R. Beasor et al. 2020). How this affects the $M_{\rm ZAMS}$ we derive here is beyond the scope of this paper.

In Section 3.4, we found that the metallicity at the site of SN 2022crv is slightly larger than solar metallicity, implying that the progenitor experienced strong stellar wind mass loss. However, the progenitor of SN 2022crv ($M_{\rm ZAMS} \approx 16$–$22\,M_\odot$) is still not massive enough to strip most of its hydrogen envelope by itself (P. A. Crowther 2007; T. Sukhbold et al. 2016), so the progenitor has to be in a binary system.

Binary interaction usually cannot fully strip the hydrogen envelope from the progenitor star (S.-C. Yoon et al. 2017; Y. Götberg et al. 2017). Whether the progenitor can shed the rest of the hydrogen depends on its wind mass-loss rate (S.-C. Yoon et al. 2017; Y. Gotberg et al. 2023). Since the progenitor of SN 2022crv likely had a high mass-loss rate ($\sim 2\times10^{-5}\,M_\odot\,{\rm yr}^{-1}$; A. Gangopadhyay et al. 2023), the orbital separation of the binary system needs to be large to prevent the hydrogen envelope from being fully stripped by wind and binary interaction (Y. Götberg et al. 2017; S.-C. Yoon et al. 2017; Y. Gotberg et al. 2023). S.-C. Yoon et al. (2017) studied a grid of SN Ib/IIb models in binary systems, and they found that at metallicity $Z = 0.02$, assuming a mass ratio of $q = 0.9$, an orbital period above 2000 days (or an initial orbital separation larger than ∼2200 $R_\odot$) is required for a progenitor with $M_{\rm ZAMS} = 18\,M_\odot$ in a binary system in order to have some remaining hydrogen envelope left. For a progenitor with $M_{\rm ZAMS} = 16\,M_\odot$, the orbital period would be larger than ∼1700 days, which is equivalent to an initial orbital separation of ∼1900 $R_\odot$. If the initial orbital separation is on the order of 100 $R_\odot$, the progenitor will lose all its hydrogen envelope with $Z \approx 0.02$. Therefore, the progenitor of SN 2022crv was likely in a binary system with an initial orbital separation larger than ∼1000 $R_\odot$.

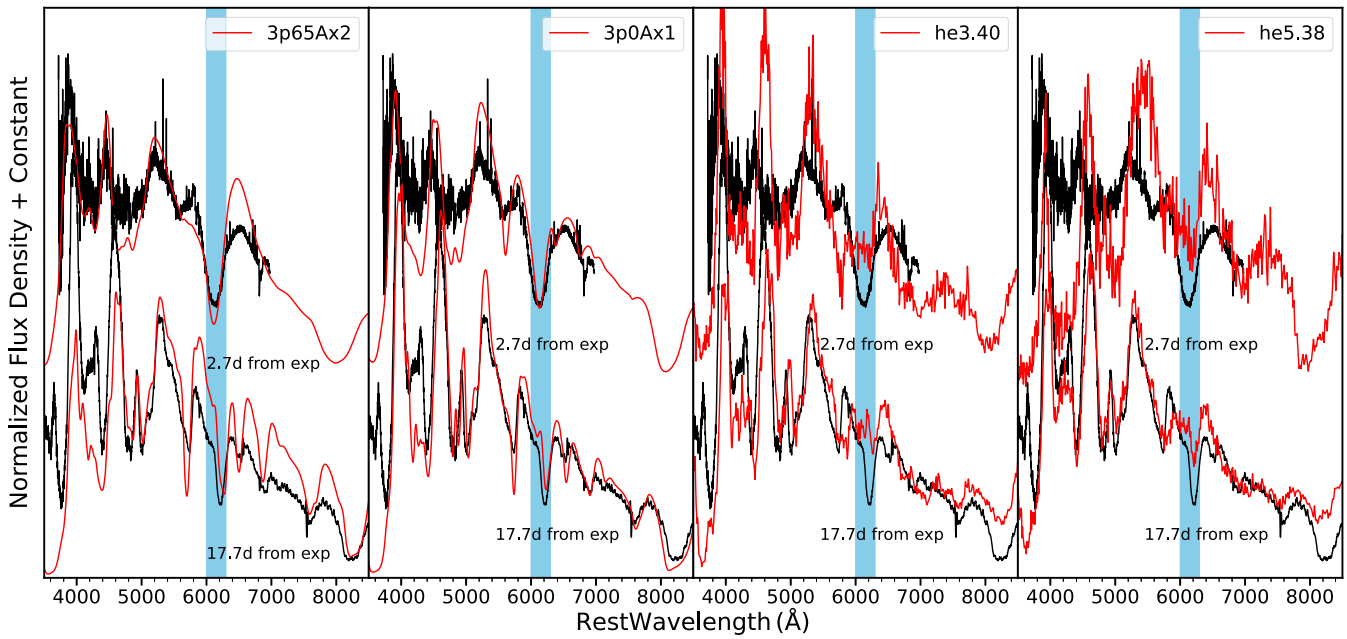

Figure 18. Comparison of the optical spectra of SN 2022crv 2.7 and 17.7 days after the explosion with models from L. Dessart et al. (2016) and S. E. Woosley et al. (2021) at similar epochs. The 6200 Å feature is marked by the blue shading. The He3.40 and He5.38 models are hydrogen-free models, while the 3p65Ax2 and 3p0Ax1 models retain a small amount of hydrogen.

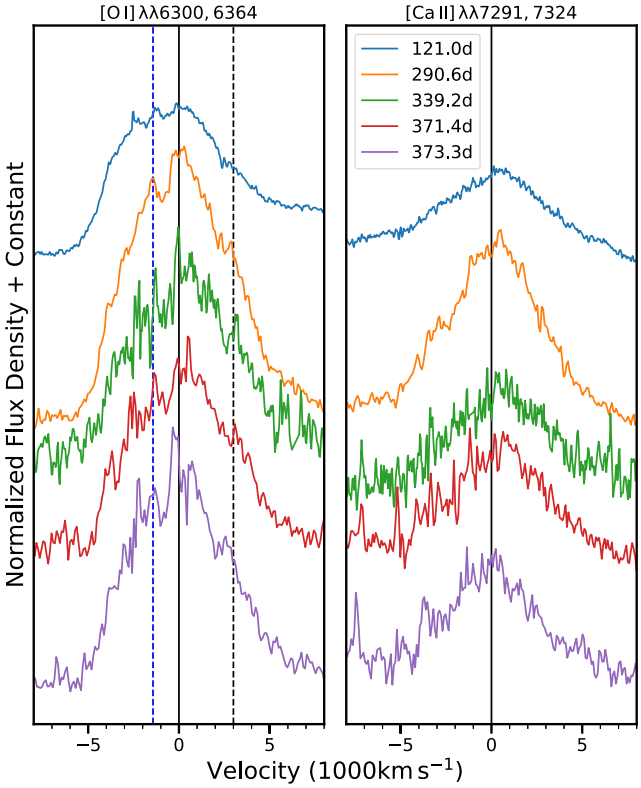

Figure 19. Late-time profile of [O I] λλ 6300, 6364 and [Ca II] λλ 7291, 7323. The phase is measured from the explosion. The zero-points for [O I] and [Ca II] are 6300 Å and 7307.5 Å, respectively, and are marked by the solid vertical lines in each panel. The black vertical dashed line in the left panel indicates 6364 Å. The blue vertical dashed line corresponds to the blueshifted peak around 6270 Å.

In conclusion, by comparing with hydrodynamic models, we found that the oxygen synthesized in the progenitor is about 1.0–1.7 $M_\odot$, and the progenitor is likely a He star with a final mass of ∼4.5–5.6 $M_\odot$ that has evolved from a 16 to 22 $M_\odot$ ZAMS star. Given the high mass-loss rate at the SN site and the very low-mass hydrogen envelope, the progenitor of SN 2022crv is likely in a binary system with a large initial orbital separation.

6.3.4. ^{56}Ni Model Fit

In order to estimate the physical parameters of the object, we applied a simple analytical model to the bolometric light curve of SN 2022crv obtained in Section 4.2. This "Arnett model" was proposed for SNe Ia (W. D. Arnett 1982; P. G. Sutherland & J. C. Wheeler 1984; E. Cappellaro et al. 1997), and can also be used for SESNe (A. Clocchiatti & J. C. Wheeler 1997; S. Valenti et al. 2008; E. Chatzopoulos et al. 2009; S. Valenti et al. 2011; E. Chatzopoulos et al. 2012; J. D. Lyman et al. 2016).

Following S. Valenti et al. (2008), we divided the light curve into photospheric and nebular phases. We assumed an optical opacity $\kappa_{\rm opt} = 0.07\ {\rm cm^2\ g^{-1}}$ and a γ-ray opacity $\kappa_\gamma = 0.027\ {\rm cm^2\ g^{-1}}$. The exact ^{56}Ni and ^{56}Co decay data presented by D. K. Nadyozhin (1994) were used for calculations. For the photospheric phase, we note that the γ-ray leakage term we adopted is slightly different from what some studies have used in the literature (e.g., E. Chatzopoulos et al. 2012).

Specifically, the bolometric light-curve evolution during the photospheric phase is written as

$$L_{\rm bol,phot}(t) = M_{\rm Ni,0}\, e^{-x^2} \times [(\epsilon_{\rm Ni} - \epsilon_{\rm Co}) \int_0^x A(z)\Gamma(z)dz + \epsilon_{\rm Co} \int_0^x B(z)\Gamma(z)dz], \quad (2)$$

where x is a function of time, $\Gamma(z)$ is the γ-ray leakage term, and $\tau_{\rm Co}$ and $\tau_{\rm Ni}$ represent the rates of energy production for ^{56}Co and ^{56}Ni (respectively). For detailed expressions of $A(z)$ and $B(z)$, we refer the reader to S. Valenti et al. (2008). The γ-ray leakage term here is a function of time, so it should be included within

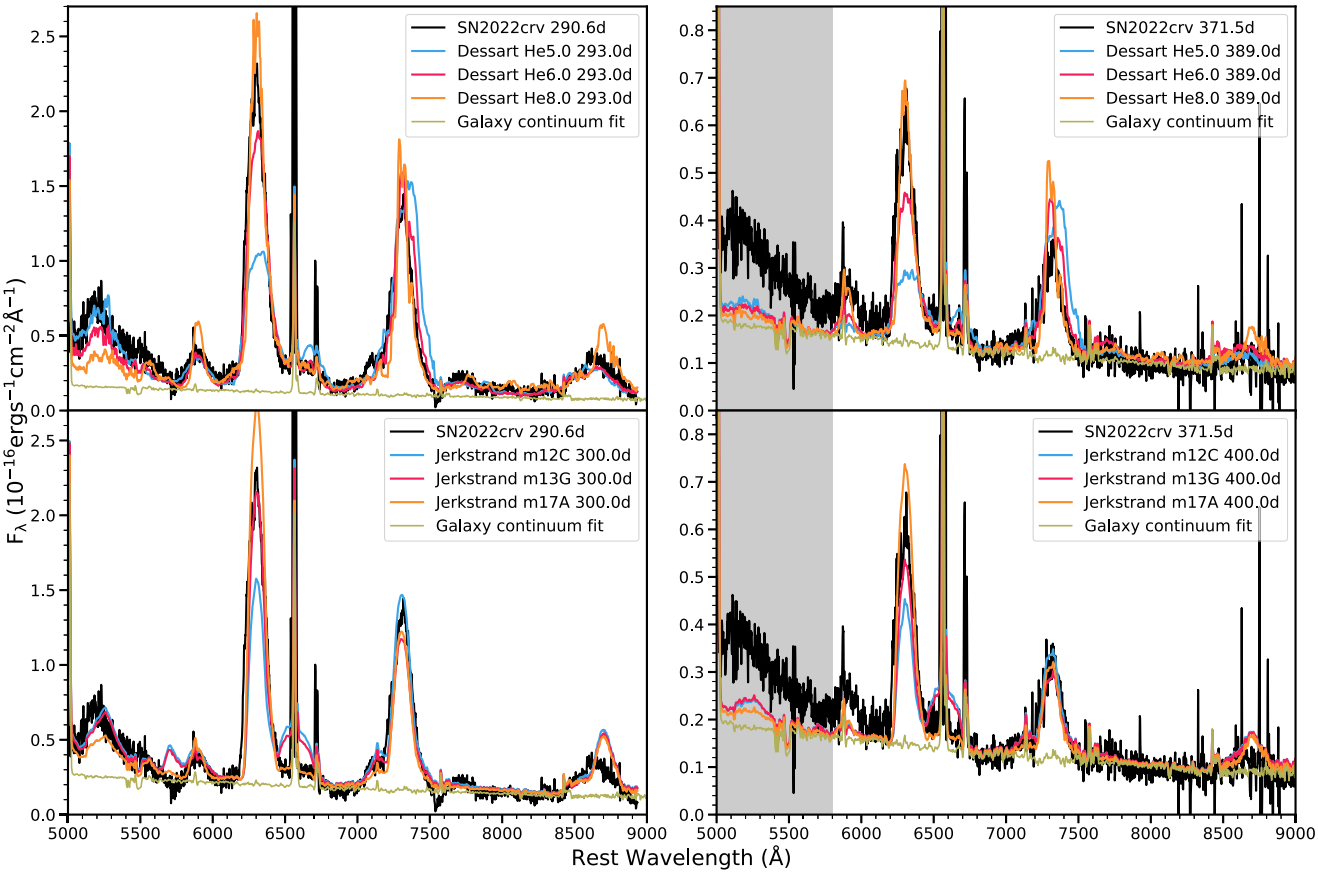

Figure 20. Comparison of the nebular spectra of SN 2022crv at 290.6 days and 371.5 days post-explosion with models from A. Jerkstrand et al. (2015) and L. Dessart et al. (2021). The spectra are contaminated by the host galaxy, so we fit them with a combination of a star-forming galaxy spectrum and the model SN spectra. For the spectrum at day 371.5, there is strong background contamination below ∼5800 Å (marked with gray shading), which makes the observed spectrum clearly depart from the assumed star-forming galaxy spectrum.

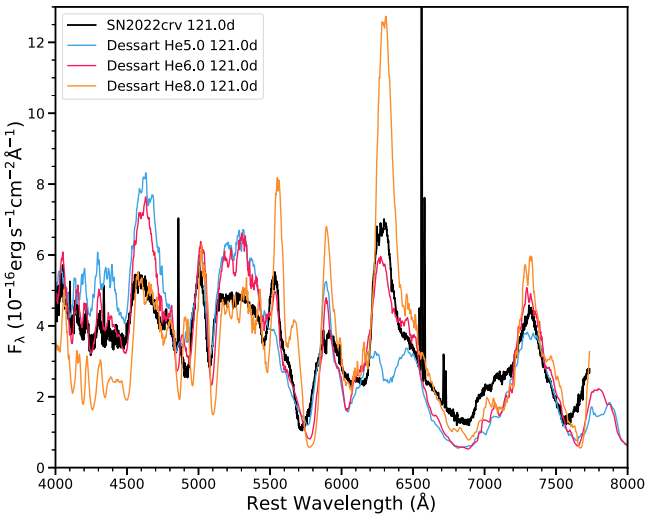

Figure 21. Comparison of the spectrum of SN 2022crv at 121 days after the explosion with models from L. Dessart et al. (2023).

the integral. Although not explicitly mentioned by S. Valenti et al. (2008), in that study, the γ-ray leakage term was actually within the integral when calculating the model light curves, as we do here.

The fit was conducted with an MCMC method. The free parameters are t_0, $M_{\rm ej}$, and $M_{\rm Ni,0}$ with uniform priors, where t_0 is the explosion epoch. The upper and lower bounds of t_0 are set to be the first detection and the last nondetection, respectively. The fitting range was chosen to be from −10 to 15 days from maximum light and 60 days post-maximum, following S. Valenti et al. (2008) and J. D. Lyman et al. (2016). The best-fitting parameters are constrained to be $M_{\rm Ni,0} = 0.21^{+0.01}_{-0.01}\ M_\odot$, $M_{\rm ej} = 4.61^{+0.07}_{-0.05}\ M_\odot$, and $E_{\rm kin} = 2.22^{+0.02}_{-0.03} \times 10^{51}$ erg. The best-fitting model is shown in Figure 22 (black line).

The model we use here cannot simultaneously reproduce the photospheric and nebular phases of the light curve of SN 2022crv. If we fit these two phases separately, the nickel mass derived from the photospheric phase will be larger than that derived from the nebular phase. The ejecta mass derived

Table 6
Nebular Spectral Models for SN 2022crv

Model	$M_{\rm ZAMS}$ ($M_\odot$)	$M_{\rm preSN}$ ($M_\odot$)	$M_{\rm He}$ ($M_\odot$)	$M_{\rm O}$ ($M_\odot$)	References
Dessart He5.0	20.8	3.81	5.0	0.592	(1)
Dessart He6.0	23.3	4.44	6.0	0.974	(1)
Dessart He8.0	27.9	5.63	8.0	1.71	(1)
Jerkstrand m12C	12	3.12	⋯	0.3	(2)
Jerkstrand m13G	13	3.52	⋯	0.52	(2)
Jerkstrand m17A	17	5.02	⋯	1.3	(2)

References. (1) S. E. Woosley (2019), T. Ertl et al. (2020), L. Dessart et al. (2021); (2) S. E. Woosley & A. Heger (2007), A. Jerkstrand et al. (2015).

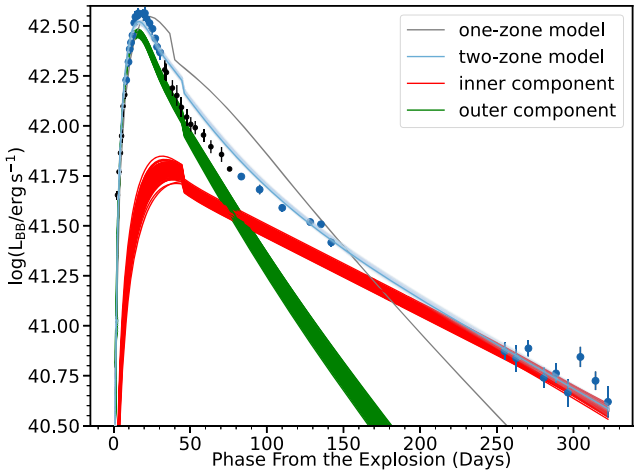

Figure 22. Arnett model fit of the bolometric light curve. The fit is done with an MCMC routine. The best-fitting results are represented by the 100 randomly chosen models drawn from the MCMC chain. The blue lines are the two-component fit and the gray lines are the one-component fit. The red lines and the green lines are the contributions from the inner region and the outer region, respectively. Only the blue points are used for the fit. The phase is shown with respect to the explosion epoch.

from the photospheric phase is too small, resulting in a low γ-ray trapping rate at late phases, leading to a too steep tail. This contradiction can be easily solved if a two-zone model is considered, one of which dominates the photospheric phase and the other contributes to the nebular phase (S. Valenti et al. 2008). In the model we adopted above, the nickel is assumed to be concentrated in the center of the progenitor. To explain the observational properties of SESNe, nickel needs to be mixed in the ejecta to some extent (S. E. Woosley & R. G. Eastman 1997; L. Dessart et al. 2012; M. C. Bersten et al. 2013; L. Dessart et al. 2015, 2016; S.-C. Yoon et al. 2019). Therefore, we adopted the two-zone model initially proposed by K. Maeda et al. (2003) that has been used for some SESNe (S. Valenti et al. 2008, 2011; Z. Cano et al. 2014). However, we note that since dust likely started to form at late phases in SN 2022crv (J. Rho et al. 2024, in preparation), dust attenuation could also contribute to this contradiction. If this is true, the late-time light curve would be brighter than what we have calculated. Therefore, the nickel mass obtained by only fitting the nebular phase would actually be larger, which would ease the contradiction.

In this model, the SN ejecta are divided into two separate zones: a high-density inner region and a low-density outer region. The nickel is assumed to be homogeneously distributed in the two regions. In this two-zone model, the free parameters are the time of explosion t_0, the total nickel mass $M_{\rm Ni,total}$, the total ejecta mass $M_{\rm ej,total}$, the kinetic energy of the inner region $E_{\rm kin,inner}$, and the mass fraction of the inner region to the whole ejecta $F_{\rm inner}$. The final best-fitting parameters are constrained to be $M_{\rm Ni,total} = 0.18^{+0.01}_{-0.01}\ M_\odot$, $M_{\rm ej,total} = 2.59^{+0.07}_{-0.08}\ M_\odot$, $E_{\rm kin,total} = 0.88^{+0.02}_{-0.02} \times 10^{51}$ erg, and $F_{\rm inner} = 0.30^{+0.01}_{-0.01}$. The two-component model does give a better fit and the best-fitting model is shown in Figure 22.

J. D. Lyman et al. (2016) analyzed a group of bolometric light curves of SESNe by fitting the Arnett model. They found that the average explosion parameters for SNe IIb are $M_{\rm Ni} = 0.11(0.04)\ M_\odot$, $M_{\rm ej} = 2.2(0.8)\ M_\odot$, and $E_{\rm kin} = 1.0(0.6) \times 10^{51}$ erg. For SNe Ib, these values are $M_{\rm Ni} = 0.17(0.16)\ M_\odot$, $M_{\rm ej} = 2.6(1.1)\ M_\odot$, and $E_{\rm kin} = 1.6(0.9) \times 10^{51}$ erg. Similar values have also been found for SESNe in more recent studies (e.g., F. Taddia et al. 2018). The parameters we derived for SN 2022crv are more similar to those of SNe Ib, but considering the uncertainties, they are consistent with those of both SNe IIb and Ib.

6.3.5. ^{56}Ni + Magnetar Fit

Magnetars are thought to be a possible energy source for SESNe (K. Maeda et al. 2007; D. Kasen & L. Bildsten 2010). We use a hybrid model in which the object is powered by both ^{56}Ni decay and magnetar spin down. The luminosity of an SN powered by a central magnetar can be written as (S. Q. Wang et al. 2015)

$$L_{\rm bol,mag} = e^{-x^2} \times \frac{E_{\rm NS}}{\tau_{\rm NS}} \times \int_0^x C(z)dz, \tag{3}$$

where $C(z) = 2ze^{z^2} \Big/ \left(1 + z\frac{\tau_m}{\tau_{\rm NS}}\right)^2 (1 - e^{-A(z\tau_m)^{-2}})$, with $A = \frac{3\kappa_\gamma M_{\rm ej}}{4\pi v^2}$.

Also,

$$E_{\rm NS} = 2 \times 10^{52} \frac{M_{\rm NS}}{1.4\ M_\odot} \left(\frac{P_0}{1\ {\rm ms}}\right)^{-2} \left(\frac{R_{\rm NS}}{10\ {\rm km}}\right)^2 {\rm erg} \tag{4}$$

and

$$\tau_{\rm NS} = 1.3 \left(\frac{B}{10^{14}\ {\rm G}}\right)^{-2} \left(\frac{P_0}{10\ {\rm ms}}\right)^2 \tag{5}$$

are the rotational energy and the spin-down timescale of the magnetar, respectively.

We found that the best-fitting model is dominated by the magnetar, and only a small amount of nickel is present in the ejecta. However, for SESNe, a certain amount of nickel should be in the ejecta and power the early part of the light curve (e.g., S. E. Woosley 2019; S. E. Woosley et al. 2021). Therefore, a magnetar-dominated model is likely not suitable in the case of SN 2022crv.

6.3.6. Search for a Progenitor Candidate

We identified a pre-explosion image at the site of SN 2022crv in the Mikulski Archive for Space Telescopes (MAST). This image was taken with the Hubble Space Telescope (HST) Wide Field Planetary Camera (WFPC2) in the F606W filter (PI: Stiavelli, SNAP-6359) on 1997 March 27.[41] We employed a 60 s r-band MODS acquisition image of the SN obtained with the LBT on 2022 March 10 to isolate the SN position in the HST image mosaic. 17 stars were identified in common between the two image data sets. Using Photutils centroiding and the PyRAF tasks `geomap` and `geotran`, we were able to locate the position with a 1σ astrometric uncertainty of 1.4 WFPC2 pixels (0.″14; see Figure 23). The SN site appears to be in a luminous complex of stars or star clusters. We subsequently ran Dolphot (A. Dolphin 2016) with point-spread-function (PSF) fitting photometry on the individual WFPC2 frames and found an object, indicated to be stellar by the routine, with brightness $m_{\rm F606W} = 24.07 \pm 0.05$ mag. Corrected by our assumed distance and extinction to SN 2022crv, this corresponds to an absolute brightness of $M_{\rm F606W} \approx -8.2$ mag.

[41] doi:10.17909/hprz-fv86

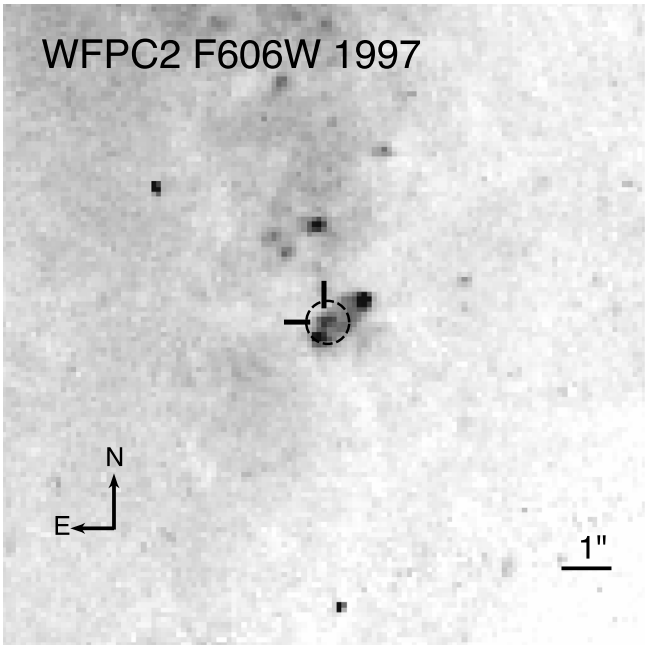

Figure 23. A portion of the HST WFPC2 F606W image mosaic from 1997 March, with the location of the SN site indicated by a dashed circle (with radius corresponding to the 3σ uncertainty in the astrometric registration using an LBT r-band image of the SN from 2022 March). A stellar-like object with $M_{\rm F606W} \approx -8.2$ mag is indicated by the black tick marks. We tentatively identify this object as the progenitor candidate. North is up, and east is to the left.

We tentatively identify this object as the progenitor candidate, although some caution should be applied, given the comparatively low HST resolution with WFPC2. Additionally, with only the single HST band, we have no knowledge of the object's color. Nevertheless, a comparison of its inferred luminosity with that of SN 2011dh's progenitor reveals interesting insights. J. R. Maund et al. (2011) found $M_{\rm F555W} \approx -7.5$ mag at the assumed distance of 7.1 Mpc. This number is adjusted to ~ -7.6 mag based on the recent Cepheid distance from G. Csörnyei et al. (2023). Similarly, S. D. Van Dyk et al. (2011) estimated $M_V^0 \approx -7.7$ mag at an assumed distance of 7.6 Mpc. Therefore, the progenitor candidate for SN 2022crv appears to be plausible, albeit somewhat more luminous than the SN 2011dh progenitor. We note, however, that J. J. Eldridge et al. (2015) found that the absolute brightness of the iPTF13bvn progenitor was at most $M_{\rm F555W} \approx -6.5$ mag, so the progenitor candidate for SN 2022crv is significantly more luminous. Whether this object is truly the SN progenitor will require confirmation, with follow-up HST observations when the SN has faded significantly (well below mag 24 in F606W).

7. Summary

We present optical and NIR observations of SN 2022crv. In general, the optical photometric and spectroscopic evolution of SN 2022crv resembles those of both SNe IIb and Ib. The object showed conspicuous high-velocity H lines at early phases around 6200 Å, which rapidly disappeared shortly after maximum brightness. The 6200 Å line in SN 2022crv is likely due to Hα at early phases and is dominated by Si II λ6355 after maximum light. The evolution of the Hα line pEW in SN 2022crv is similar to those of SNe IIb at early phases, but falls into the SN Ib category shortly after maximum light. In addition, we applied an SVM classification method to the spectra ranging from -15 days to 15 days relative to peak brightness, classifying SN 2022crv as an SN IIb before -10 days and an SN Ib afterward. This makes SN 2022crv a transitional object on the continuum between SNe Ib and IIb, providing additional clues to the proposed continuum between these two SN subtypes.

We found that a hydrogen envelope mass of $\sim 10^{-3}\ M_\odot$ in the progenitor can reproduce the behaviors of the H lines in SN 2022crv, and the progenitor is constrained to be a He star with a final mass of $\sim$4.5–5.6 $M_\odot$ evolving from a $\sim$16 to 22 $M_\odot$ ZAMS star in a binary system. Since the progenitor of SN 2022crv likely experienced relatively strong mass loss, an initial orbital separation of the binary system larger than $\sim 1000\ R_\odot$ is needed in order to retain a small amount of the hydrogen envelope. We found that the bolometric light curve of SN 2022crv can be best fitted by a model with a nickel mass of $0.18^{+0.01}_{-0.01}\ M_\odot$, $M_{\rm ej}$ of $2.59^{+0.07}_{-0.08}\ M_\odot$, and $E_{\rm kin}$ of $0.88^{+0.02}_{-0.02} \times 10^{51}$ erg.

The NIR spectroscopic evolution of SN 2022crv is generally similar to that of other SNe IIb/Ib. However, an extra absorption feature is observed in the NIR spectra, near the blue side of the He I λ1.083 μm line, referred to as feature A in this paper. To the best of our knowledge, feature A has never been observed in other SNe IIb/Ib. We found that this line is most likely from Sr II λ1.0327 μm, but we could not safely exclude Fe I λ1.05 μm and S I λ1.0457 μm. Future detailed modeling is required to further investigate the origin of feature A.

The peculiar features observed in the optical and NIR spectra of SN 2022crv illustrate that SESNe still have many unsolved mysteries. This emphasizes the importance of obtaining NIR spectra and the early discovery of SESNe. As the number of SESNe characterized with detailed data sets increases, the gap between SNe IIb and SNe Ib could be filled, giving us a comprehensive picture of the evolutionary channel and history of the SESN progenitors.

Acknowledgments

We thank Luc Dessart for providing the model spectra and beneficial discussions, as well as J. Craig Wheeler, Emmanouil Chatzopoulos, and Jozsef Vinkó for useful discussions. We acknowledge Stanford Woosley for generating and providing the model spectra, and Sung-Chul Yoon for providing the model light curves. We are grateful to the staff at the various observatories where data were obtained. Y.D. would like to thank the hospitality and support of L.Z. in Philadelphia during the completion of this paper.

Research by Y.D., S.V., N.M.R, E.H., and D.M. is supported by the National Science Foundation (NSF) grant AST-2008108. Time-domain research by the University of Arizona team and D. J.S. is supported by NSF grants AST-1821987, 1813466, 1908972, 2108032, and 2308181, and by the Heising-Simons Foundation under grant #2020-1864. M.M. acknowledges support in part from ADAP grant 80NSSC22K0486, from NSF grant AST-2206657, and from HST grant GO-16656. This work makes use of data from the Las Cumbres Observatory global telescope network. The Las Cumbres Observatory group is supported by NSF grants AST-1911151 and AST-1911225. N.E.R. acknowledges support from the PRIN-INAF 2022, "Shedding light on the nature of gap transients: from the observations to the models." K.A.B. is supported by an LSSTC Catalyst Fellowship; this publication was thus made possible

through the support of Grant 62192 from the John Templeton Foundation to LSSTC. The opinions expressed in this publication are those of the authors and do not necessarily reflect the views of LSSTC or the John Templeton Foundation. L.A.K. acknowledges support by NASA FINESST fellowship 80NSSC22K1599. S.M. acknowledges support from the Magnus Ehrnrooth Foundation and the Vilho, Yrjö and Kalle Väisälä Foundation. L.G. acknowledges financial support from the Spanish Ministerio de Ciencia e Innovación (MCIN), the Agencia Estatal de Investigación (AEI) 10.13039/501100011033, and the European Social Fund (ESF) "Investing in your future" under the 2019 Ramón y Cajal program RYC2019-027683-I and the PID2020-115253GA-I00 HOSTFLOWS project, from Centro Superior de Investigaciones Científicas (CSIC) under the PIE project 20215AT016, and the program Unidad de Excelencia María de Maeztu CEX2020-001058-M. M.D.S. is funded by the Independent Research Fund Denmark (IRFD) via Project 2 grant 10.46540/2032-00022B. The SALT data presented here were obtained through Rutgers University programs 2021-1-MLT-007 and 2022-1-MLT-004 (PI S.W.J.). A.V.F.'s research group at UC Berkeley acknowledges financial assistance from NASA/HST grant AR-14259 from STScI, the Christopher R. Redlich Fund, Gary and Cynthia Bengier, Clark and Sharon Winslow, Alan Eustace (W.Z. is a Bengier-Winslow-Eustace Specialist in Astronomy), William Draper, Timothy and Melissa Draper, Briggs and Kathleen Wood, Sanford Robertson (T.G.B. is a Draper-Wood-Robertson Specialist in Astronomy), and numerous other donors.

Based in part on observations obtained at the international Gemini Observatory, a program of NSF's NOIRLab, which is managed by the Association of Universities for Research in Astronomy (AURA) under a cooperative agreement with the NSF. On behalf of the Gemini Observatory partnership: the National Science Foundation (United States), National Research Council (Canada), Agencia Nacional de Investigación y Desarrollo (Chile), Ministerio de Ciencia, Tecnología e Innovación (Argentina), Ministério da Ciência, Tecnologia, Inovações e Comunicações (Brazil), and Korea Astronomy and Space Science Institute (Republic of Korea). This work was enabled by observations made from the Gemini North telescope, located within the Maunakea Science Reserve and adjacent to the summit of Maunakea. We are grateful for the privilege of observing the Universe from a place that is unique in both its astronomical quality and its cultural significance.

Some of the data reported here were obtained at the MMT Observatory, a joint facility of the University of Arizona and the Smithsonian Institution. This paper uses data gathered with the 6.5 m Magellan telescopes at Las Campanas Observatory, Chile. The LBT is an international collaboration among institutions in the United States, Italy, and Germany. LBT Corporation Members are The University of Arizona on behalf of the Arizona Board of Regents; Istituto Nazionale di Astrofisica, Italy; LBT Beteiligungsgesellschaft, Germany, representing the Max-Planck Society, The Leibniz Institute for Astrophysics Potsdam, and Heidelberg University; The Ohio State University, and The Research Corporation, on behalf of The University of Notre Dame, University of Minnesota and University of Virginia.

This research is based in part on observations made with the NASA/ESA Hubble Space Telescope obtained from the Space Telescope Science Institute, which is operated by the Association of Universities for Research in Astronomy, Inc., under NASA contract NAS 5-26555. The data were obtained from MAST at the Space Telescope Science Institute. The specific observations analyzed can be accessed via DOI: 10.17909/hprz-fv86.

Based in part on observations made with GTC, installed at the Spanish Observatorio del Roque de los Muchachos of the Instituto de Astrofísica de Canarias, on the island of La Palma. This work is partly based on data obtained with the instrument OSIRIS, built by a Consortium led by the Instituto de Astrofísica de Canarias in collaboration with the Instituto de Astronomía of the Universidad Autónoma de México. OSIRIS was funded by GRANTECAN and the National Plan of Astronomy and Astrophysics of the Spanish Government.

KAIT and its ongoing operation at Lick Observatory were made possible by donations from Sun Microsystems, Inc., the Hewlett-Packard Company, AutoScope Corporation, Lick Observatory, the U.S. NSF, the University of California, the Sylvia & Jim Katzman Foundation, and the TABASGO Foundation. A major upgrade of the Kast spectrograph on the Shane 3 m telescope at Lick Observatory, led by Brad Holden, was made possible through generous gifts from the Heising-Simons Foundation, William and Marina Kast, and the University of California Observatories. We thank UC Berkeley undergraduate students Ivan Altunin, Kate Bostow, Kingsley Ehrich, Nachiket Girish, Neil Pichay, and James Sunseri for their efforts in taking Lick/Nickel data. Research at Lick Observatory is partially supported by a generous gift from Google.

Some of the data presented herein were obtained at the W. M. Keck Observatory, which is operated as a scientific partnership among the California Institute of Technology, the University of California, and NASA; the observatory was made possible by the generous financial support of the W. M. Keck Foundation.

This research has made use of the NASA/IPAC Extragalactic Database (NED), which is funded by the National Aeronautics and Space Administration and operated by the California Institute of Technology.

This research made use of Photutils, an Astropy package for the detection and photometry of astronomical sources (L. Bradley et al. 2022).

Facilities: ADS, CTIO:PROMPT, Nickel, KAIT, ATLAS, LCOGT (SBIG, Sinistro, FLOYDS), Gemini:Gillett (GMOS), Keck:I (LRIS), Keck:II (DEIMOS, NIRES), LCOGT (Sinistro), MMT (Binospec, MMIRS), NED, SALT (RSS), Shane (Kast), SOAR (Goodman), Swift (UVOT), Magellan:Baade (IMACS, FIRE), Magellan:Clay (LDSS3), UH:2.2m (SNIFS), Bok (B&C), LBT (MODS).

Software: Astropy (Astropy Collaboration et al. 2013, 2018), HOTPANTS (A. Becker 2015), Matplotlib (J. D. Hunter 2007), NumPy (C. R. Harris et al. 2020), PYRAF (Science Software Branch at STScI 2012), Pandas (W. McKinney 2010), SciPy (P. Virtanen et al. 2020), SWarp (E. Bertin et al. 2002), HOTPANTS (A. Becker 2015), LCOGTSNpipe (S. Valenti et al. 2016), Light Curve Fitting (G. Hosseinzadeh & S. Gomez 2020), PypeIt (J. X. Prochaska et al. 2020b).

Appendix A
Photometric Data Reduction

The photometric data from the Las Cumbres Observatory were reduced using the PyRAF-based photometric reduction pipeline LCOGTSNPIPE (S. Valenti et al. 2016). This pipeline uses a low-order polynomial fit to remove the background and

calculates instrumental magnitudes using a standard PSF-fitting technique. Apparent magnitudes were calibrated using the AAVSO Photometric All-Sky Survey (APASS[42]) (g, r, i) and Landolt (U, B, V) catalogs (A. U. Landolt 1992).

Unfiltered (*Open*) DLT40 images were processed with a PyRAF-based pipeline. Background contamination was removed by subtracting a reference image, and the aperture photometry was extracted from the subtracted images. The final photometry is calibrated to the r band using the APASS catalog.

The ATLAS survey is carried out primarily in two filters, cyan and orange, roughly equivalent to Pan-STARRS filters $g+r$ and $r+i$, respectively. Typically, four sets of 30 s exposures are taken for each field within a 1 hr timeframe. The images are processed and difference imaging is performed in real time to enable the rapid discovery of transients in the data stream (K. W. Smith et al. 2020). We obtained the forced photometry at the SN position from the ATLAS forced photometry server (L. Shingles et al. 2021). We stacked the individual flux measurements for each nightly quad into a single measurement in order to improve the signal-to-noise ratio, and to obtain deeper upper limits for the prediscovery nondetections.

The images obtained with KAIT and Nickel at Lick Observatory were reduced using a custom pipeline[43] detailed by B. E. Stahl et al. (2019). PSF photometry was obtained using DAOPHOT (P. B. Stetson 1987) from the IDL Astronomy User's Library.[44] Several nearby stars were chosen from the Pan-STARRS1[45] catalog for calibration. Their magnitudes were first transformed into Landolt magnitudes using the empirical prescription presented by J. L. Tonry et al. (2012), then transformed to the KAIT/Nickel natural system. The final results were transformed to the standard system using local sequence stars and color terms for KAIT4 and Nickel2 (B. E. Stahl et al. 2019).

Swift images were reduced using the High-Energy Astrophysics software. The background was measured from a region away from any stars. Zero-points were chosen from A. A. Breeveld et al. (2011) with time-dependent sensitivity corrections updated in 2020.

Appendix B
Spectroscopic Data Reduction

FLOYDS spectra were reduced following standard procedures using the FLOYDS pipeline (S. Valenti et al. 2014). The IMACS Baade spectra were reduced using standard methods and IRAF routines,[46] as described by M. Hamuy et al. (2006). The UH88 data were obtained with SNIFS and reduced using the method outlined by M. A. Tucker et al. (2022). The SALT spectra were reduced using a custom long-slit pipeline based on the PySALT package (S. M. Crawford et al. 2010). The NOT ALFOSC spectrum was reduced using the PypeIt pipeline (J. X. Prochaska et al. 2020a, 2020b, 2020)

The spectrum taken with GMOS as part of our program GN-22A-Q-135 used the B600 grating and a 1.″5 slit. Data were reduced with the `DRAGONS` (Data Reduction for Astronomy from Gemini Observatory North and South) package (K. Labrie et al. 2019), using the recipe for GMOS long-slit reductions. This includes bias correction, flat-fielding, wavelength calibration, and flux calibration.

The spectrum obtained with LDSS3 was reduced using IRAF, including bias subtraction, flat-fielding, cosmic-ray rejection, local sky subtraction, and extraction of one-dimensional (1D) spectra. The slit was aligned along the parallactic angle (A. V. Filippenko 1982) to minimize differential light losses, and flux calibration was done using a spectrophotometric standard taken that night at similar airmass.

The Keck NIRES data were reduced following standard procedures described in the IDL package `Spextools` version 5.0.2 for NIRES (M. C. Cushing et al. 2004). The extracted 1D spectrum was flux calibrated and also corrected for telluric features with `Xtellcorr` (W. D. Vacca et al. 2003) version 5.0.2 for NIRES, making use of an A0 V standard star close in time and at similar airmass to the science target.

The two spectra taken with the Kast double spectrograph (J. S. Miller & R. P. S. Stone 1994) mounted on the Shane 3 m telescope at Lick Observatory utilized the 2″ slit, 600/4310 grism, and 300/7500 grating. This instrument configuration has a combined wavelength range of ∼3500–10500 Å, and a spectral resolving power of $R \approx 800$. To minimize slit losses caused by atmospheric dispersion (A. V. Filippenko 1982), the slit was oriented at or near the parallactic angle. The data were reduced following standard techniques for CCD processing and spectrum extraction (J. M. Silverman et al. 2012) utilizing IRAF (D. Tody 1986) routines and custom Python and IDL codes.[47] Low-order polynomial fits to comparison-lamp spectra were used to calibrate the wavelength scale, and small adjustments derived from night-sky lines in the target frames were applied. The spectra were flux calibrated using observations of appropriate spectrophotometric standard stars observed on the same night, at similar airmasses, and with an identical instrument configuration.

The NIR spectrum obtained using FIRE mounted on the 6.5 m Magellan Baade telescope at Las Campanas Observatory, Chile, was taken in the high-throughput prism mode with a 0.″6 slit. For telluric correction, an A0 V star was observed close in time and at a similar airmass to the science target. The spectra were reduced using the IDL pipeline `firehose` (R. A. Simcoe et al. 2013). Details of the observation setup and reduction were outlined by E. Y. Hsiao et al. (2019).

NIR spectra were obtained with the MMT and MMIRS on the 6.5 m MMT Observatory telescope on Mt. Hopkins at the Smithsonian's Fred Lawrence Whipple Observatory using a 1.″0 slit in both the zJ and HK (with the high-throughput $HK3$ filter) spectroscopic modes. The data were reduced using the automated MMIRS pipeline (I. Chilingarian et al. 2015). Telluric corrections and absolute flux calibrations were performed using observations of the A0 V star HD 72033 close in time and at similar airmass to the science target. We employed the method of W. D. Vacca et al. (2003) implemented in the IDL tool XTELLCOR_GENERAL developed by M. C. Cushing et al. (2004) as part of the `Spextool` package.

The Keck LRIS optical spectra were reduced in the standard manner with PYPEIT (J. X. Prochaska et al. 2020a,2020b, 2020).

[42] https://www.aavso.org/apass
[43] https://github.com/benstahl92/LOSSPhotPypeline
[44] http://idlastro.gsfc.nasa.gov/
[45] http://archive.stsci.edu/panstarrs/search.php
[46] IRAF was distributed by the National Optical Astronomy Observatory, which was operated by AURA under cooperative agreement with the National Science Foundation.
[47] https://github.com/ishivvers/TheKastShiv

The GTC spectrum was reduced following standard procedures with PYRAF routines via the graphical user interface FOSCGUI.[48] The 2D frames were corrected for bias and flat-fielded before the 1D spectral extraction. We wavelength calibrated the spectra via comparison with comparison-lamp spectra and calibrated the flux using spectrophotometric standard stars. These also helped in removing the strongest telluric absorption bands present in the spectrum. Finally, the absolute flux calibration of the spectrum was cross-checked against the broadband photometry.

ORCID iDs

Yize Dong (董一泽) https://orcid.org/0000-0002-7937-6371
Stefano Valenti https://orcid.org/0000-0001-8818-0795
Chris Ashall https://orcid.org/0000-0002-5221-7557
Marc Williamson https://orcid.org/0000-0003-2544-4516
David J. Sand https://orcid.org/0000-0003-4102-380X
Schuyler D. Van Dyk https://orcid.org/0000-0001-9038-9950
Alexei V. Filippenko https://orcid.org/0000-0003-3460-0103
Saurabh W. Jha https://orcid.org/0000-0001-8738-6011
Michael Lundquist https://orcid.org/0000-0001-9589-3793
Maryam Modjaz https://orcid.org/0000-0001-7132-0333
Jennifer E. Andrews https://orcid.org/0000-0003-0123-0062
Jacob E. Jencson https://orcid.org/0000-0001-5754-4007
Griffin Hosseinzadeh https://orcid.org/0000-0002-0832-2974
Jeniveve Pearson https://orcid.org/0000-0002-0744-0047
Lindsey A. Kwok https://orcid.org/0000-0003-3108-1328
Teresa Boland https://orcid.org/0000-0002-1250-4690
Eric Y. Hsiao https://orcid.org/0000-0003-1039-2928
Nathan Smith https://orcid.org/0000-0001-5510-2424
Nancy Elias-Rosa https://orcid.org/0000-0002-1381-9125
Shubham Srivastav https://orcid.org/0000-0003-4524-6883
Stephen Smartt https://orcid.org/0000-0002-8229-1731
Michael Fulton https://orcid.org/0000-0003-1916-0664
WeiKang Zheng https://orcid.org/0000-0002-2636-6508
Thomas G. Brink https://orcid.org/0000-0001-5955-2502
Melissa Shahbandeh https://orcid.org/0000-0002-9301-5302
K. Azalee Bostroem https://orcid.org/0000-0002-4924-444X
Emily Hoang https://orcid.org/0000-0003-2744-4755
Daryl Janzen https://orcid.org/0000-0003-0549-3281
Darshana Mehta https://orcid.org/0009-0008-9693-4348
Nicolas Meza https://orcid.org/0000-0002-7015-3446
Manisha Shrestha https://orcid.org/0000-0002-4022-1874
Samuel Wyatt https://orcid.org/0000-0003-2732-4956
Katie Auchettl https://orcid.org/0000-0002-4449-9152
Christopher R. Burns https://orcid.org/0000-0003-4625-6629
Joseph Farah https://orcid.org/0000-0003-4914-5625
Lluís Galbany https://orcid.org/0000-0002-1296-6887
Estefania Padilla Gonzalez https://orcid.org/0000-0003-0209-9246
Joshua Haislip https://orcid.org/0000-0002-6703-805X
Jason T. Hinkle https://orcid.org/0000-0001-9668-2920
D. Andrew Howell https://orcid.org/0000-0003-4253-656X
Thomas De Jaeger https://orcid.org/0000-0001-6069-1139
Vladimir Kouprianov https://orcid.org/0000-0003-3642-5484
Sahana Kumar https://orcid.org/0000-0001-8367-7591
Jing Lu https://orcid.org/0000-0002-3900-1452
Curtis McCully https://orcid.org/0000-0001-5807-7893
Shane Moran https://orcid.org/0000-0001-5221-0243
Nidia Morrell https://orcid.org/0000-0003-2535-3091
Megan Newsome https://orcid.org/0000-0001-9570-0584
Craig Pellegrino https://orcid.org/0000-0002-7472-1279
Abigail Polin https://orcid.org/0000-0002-1633-6495
Daniel E. Reichart https://orcid.org/0000-0002-5060-3673
B. J. Shappee https://orcid.org/0000-0003-4631-1149
Maximilian D. Stritzinger https://orcid.org/0000-0002-5571-1833
Giacomo Terreran https://orcid.org/0000-0003-0794-5982
M. A. Tucker https://orcid.org/0000-0002-2471-8442

[48] FOSCGUI is a graphic user interface aimed at extracting SN spectroscopy and photometry obtained with FOSC-like instruments. It was developed by E. Cappellaro. A package description can be found at http://sngroup.oapd.inaf.it/foscgui.html.

References

Aldering, G., Humphreys, R. M., & Richmond, M. 1994, AJ, 107, 662
Allende Prieto, C., Lambert, D. L., & Asplund, M. 2001, ApJL, 556, L63
Allington-Smith, J., Breare, M., Ellis, R., et al. 1994, PASP, 106, 983
Andrews, J. E., Lundquist, M., Sand, D. J., et al. 2022, TNSCR, 2022-454
Arnett, W. D. 1982, ApJ, 253, 785
Asplund, M., Grevesse, N., Sauval, A. J., & Scott, P. 2009, ARA&A, 47, 481
Astropy Collaboration, Price-Whelan, A. M., Sipőcz, B. M., et al. 2018, AJ, 156, 123
Astropy Collaboration, Robitaille, T. P., Tollerud, E. J., et al. 2013, A&A, 558, A33
Beasor, E. R., Davies, B., Smith, N., et al. 2020, MNRAS, 492, 5994
Becker, A., 2015 HOTPANTS: High Order Transform of PSF ANd Template Subtraction, Astrophysics Source Code Library, ascl:1504.004
Bersten, M. C., Tanaka, M., Tominaga, N., Benvenuto, O. G., & Nomoto, K. 2013, ApJ, 767, 143
Bertin, E., Mellier, Y., Radovich, M., et al. 2002, in ASP Conf. Ser. 281, Astronomical Data Analysis Software and Systems XI, ed. D. A. Bohlender, D. Durand, & T. H. Handley (San Francisco, CA: ASP), 228
Blondin, S., & Tonry, J. L. 2007, ApJ, 666, 1024
Bradley, L., Sipőcz, B., Robitaille, T., et al. 2022, astropy/photutils: v1.5.0, Zenodo, doi:10.5281/zenodo.6825092
Branch, D., Benetti, S., Kasen, D., et al. 2002, ApJ, 566, 1005
Breeveld, A. A., Landsman, W., Holland, S. T., et al. 2011, in AIP Conf. Ser. 1358, Gamma Ray Bursts 2010, ed. J. E. McEnery, J. L. Racusin, & N. Gehrels (Melville, NY: AIP), 373
Brethauer, D., Margutti, R., Milisavljevic, D., et al. 2022, ApJ, 939, 105
Brown, T. M., Baliber, N., Bianco, F. B., et al. 2013, PASP, 125, 1031
Burns, C., Hsiao, E., Suntzeff, N., et al. 2021, ATel, 14441, 1
Cano, Z., Maeda, K., & Schulze, S. 2014, MNRAS, 438, 2924
Cappellaro, E., Mazzali, P. A., Benetti, S., et al. 1997, A&A, 328, 203
Cepa, J., Aguiar-Gonzalez, M., Gonzalez-Escalera, V., et al. 2000, Proc. SPIE, 4008, 623
Chatzopoulos, E., Wheeler, J. C., & Vinko, J. 2009, ApJ, 704, 1251
Chatzopoulos, E., Wheeler, J. C., & Vinko, J. 2012, ApJ, 746, 121
Chevalier, R. A., & Soderberg, A. M. 2010, ApJL, 711, L40
Chilingarian, I., Beletsky, Y., Moran, S., et al. 2015, PASP, 127, 406
Clemens, J. C., Crain, J. A., & Anderson, R. 2004, Proc. SPIE, 5492, 331
Clocchiatti, A., & Wheeler, J. C. 1997, ApJ, 491, 375
Crawford, S. M., Still, M., Schellart, P., et al. 2010, Proc. SPIE, 7737, 773725
Crowther, P. A. 2007, ARA&A, 45, 177
Csörnyei, G., Anderson, R. I., Vogl, C., et al. 2023, A&A, 678, A44
Curti, M., Mannucci, F., Cresci, G., & Maiolino, R. 2020, MNRAS, 491, 944
Cushing, M. C., Vacca, W. D., & Rayner, J. T. 2004, PASP, 116, 362
Davis, S., Hsiao, E. Y., Ashall, C., et al. 2019, ApJ, 887, 4
Deng, J. S., Qiu, Y. L., Hu, J. Y., Hatano, K., & Branch, D. 2000, ApJ, 540, 452
Dessart, L., & Hillier, D. J. 2005, A&A, 439, 671
Dessart, L., Hillier, D. J., Li, C., & Woosley, S. 2012, MNRAS, 424, 2139
Dessart, L., Hillier, D. J., Livne, E., et al. 2011, MNRAS, 414, 2985
Dessart, L., Hillier, D. J., Sukhbold, T., Woosley, S. E., & Janka, H. T. 2021, A&A, 656, A61
Dessart, L., Hillier, D. J., Woosley, S., et al. 2015, MNRAS, 453, 2189
Dessart, L., Hillier, D. J., Woosley, S., et al. 2016, MNRAS, 458, 1618
Dessart, L., Hillier, D. J., Woosley, S. E., & Kuncarayakti, H. 2023, A&A, 677, A7
Dolphin, A. 2016 DOLPHOT: Stellar photometry, Astrophysics Source Code Library, ascl:1608.013
Dong, Y., Valenti, S., Sand, D. J., et al. 2022, TNSTR 2022-448
Dressler, A., Bigelow, B., Hare, T., et al. 2011, PASP, 123, 288

Drout, M. R., Soderberg, A. M., Gal-Yam, A., et al. 2011, ApJ, 741, 97
Drout, M. R., Milisavljevic, D., Parrent, J., et al. 2016, ApJ, 821, 57
Eldridge, J. J., Fraser, M., Maund, J. R., & Smartt, S. J. 2015, MNRAS, 446, 2689
Eldridge, J. J., Fraser, M., Smartt, S. J., Maund, J. R., & Crockett, R. M. 2013, MNRAS, 436, 774
Eldridge, J. J., & Tout, C. A. 2004, MNRAS, 353, 87
Elmhamdi, A., Danziger, I. J., Branch, D., et al. 2006, A&A, 450, 305
Elmhamdi, A., Danziger, I. J., Cappellaro, E., et al. 2004, A&A, 426, 963
Ergon, M., Sollerman, J., Fraser, M., et al. 2014, A&A, 562, A17
Ertl, T., Woosley, S. E., Sukhbold, T., & Janka, H. T. 2020, ApJ, 890, 51
Fabricant, D., Fata, R., Epps, H., et al. 2019, PASP, 131, 075004
Fang, Q., Maeda, K., Kuncarayakti, H., et al. 2022, ApJ, 928, 151
Filippenko, A. V. 1982, PASP, 94, 715
Filippenko, A. V. 1988, AJ, 96, 1941
Filippenko, A. V. 1997, ARA&A, 35, 309
Filippenko, A. V., Li, W. D., Treffers, R. R., & Modjaz, M. 2001, in ASP Conf. Ser. 246, IAU Colloq. 183: Small Telescope Astronomy on Global Scales, ed. B. Paczynski, W.-P. Chen, & C. Lemme (San Francisco, CA: ASP), 121
Filippenko, A. V., Matheson, T., & Ho, L. C. 1993, ApJL, 415, L103
Folatelli, G., Bersten, M. C., Kuncarayakti, H., et al. 2014, ApJ, 792, 7
Folatelli, G., Van Dyk, S. D., Kuncarayakti, H., et al. 2016, ApJL, 825, L22
Fremling, C., Sollerman, J., Taddia, F., et al. 2014, A&A, 565, A114
Fremling, C., Sollerman, J., Kasliwal, M. M., et al. 2018, A&A, 618, A37
Fryer, C. L., Mazzali, P. A., Prochaska, J., et al. 2007, PASP, 119, 1211
Gal-Yam, A. 2017, Handbook of Supernovae (Berlin: Springer), 195
Galbany, L., Anderson, J. P., Sánchez, S. F., et al. 2018, ApJ, 855, 107
Gangopadhyay, A., Maeda, K., Singh, A., et al. 2023, ApJ, 957, 100
Gehrels, N., Chincarini, G., Giommi, P., et al. 2004, ApJ, 611, 1005
Gilkis, A., & Arcavi, I. 2022, MNRAS, 511, 691
Gimeno, G., Roth, K., Chiboucas, K., et al. 2016, Proc. SPIE, 9908, 99082S
Götberg, Y., de Mink, S. E., & Groh, J. H. 2017, A&A, 608, A11
Götberg, Y., de Mink, S. E., Groh, J. H., et al. 2018, A&A, 615, A78
Gotberg, Y., Drout, M. R., Ji, A. P., et al. 2023, ApJ, 959, 125
Green, R., Schmidt, G., Oey, S., Wittman, D., & Hall, P. 1995, Steward Observatory 2.3-m Boller and Chivens Spectrograph Manual, http://james.as.arizona.edu/~psmith/90inch/bcman/html/bcman.html
Hachinger, S., Mazzali, P. A., Taubenberger, S., et al. 2012, MNRAS, 422, 70
Hamuy, M., Maza, J., Pinto, P. A., et al. 2002, AJ, 124, 417
Hamuy, M., Folatelli, G., Morrell, N. I., et al. 2006, PASP, 118, 2
Harkness, R. P., Wheeler, J. C., Margon, B., et al. 1987, ApJ, 317, 355
Harris, C. R., Millman, K. J., van der Walt, S. J., et al. 2020, Natur, 585, 357
Hiramatsu, D., Howell, D. A., Moriya, T. J., et al. 2021, ApJ, 913, 55
Holmbo, S., Stritzinger, M. D., Karamehmetoglu, E., et al. 2023, A&A, 675, A83
Hook, I. M., Jørgensen, I., Allington-Smith, J. R., et al. 2004, PASP, 116, 425
Hosseinzadeh, G., & Gomez, S. 2020, Light Curve Fitting, v0.2.0, Zenodo, doi:10.5281/zenodo.4312178
Houck, J. C., & Fransson, C. 1996, ApJ, 456, 811
Hsiao, E. Y., Phillips, M. M., Marion, G. H., et al. 2019, PASP, 131, 014002
Hunter, D. J., Valenti, S., Kotak, R., et al. 2009, A&A, 508, 371
Hunter, J. D. 2007, CSE, 9, 90
James, S., & Baron, E. 2010, ApJ, 718, 957
Jerkstrand, A., Ergon, M., Smartt, S. J., et al. 2015, A&A, 573, A12
Jerkstrand, A., Fransson, C., Maguire, K., et al. 2012, A&A, 546, A28
Kasen, D., & Bildsten, L. 2010, ApJ, 717, 245
Kilpatrick, C. D., Foley, R. J., Abramson, L. E., et al. 2017, MNRAS, 465, 4650
Kilpatrick, C. D., Drout, M. R., Auchettl, K., et al. 2021, MNRAS, 504, 2073
Kinney, A. L., Calzetti, D., Bohlin, R. C., et al. 1996, ApJ, 467, 38
Kuncarayakti, H., Maeda, K., Bersten, M. C., et al. 2015, A&A, 579, A95
Labrie, K., Anderson, K., Cárdenes, R., Simpson, C., & Turner, J. E. H. 2019, in ASP Conf. Ser. 523, Astronomical Data Analysis Software and Systems XXVII, ed. P. J. Teuben et al. (San Francisco, CA: ASP), 321
Landolt, A. U. 1992, AJ, 104, 340
Lantz, B., Aldering, G., Antilogus, P., et al. 2004, Proc. SPIE, 5249, 146
Li, W., Filippenko, A. V., Chornock, R., & Jha, S. 2003, PASP, 115, 844
Liu, Y.-Q., Modjaz, M., Bianco, F. B., & Graur, O. 2016, ApJ, 827, 90
Lyman, J. D., Bersier, D., James, P. A., et al. 2016, MNRAS, 457, 328
Maeda, K., Mazzali, P. A., Deng, J., et al. 2003, ApJ, 593, 931
Maeda, K., Tanaka, M., Nomoto, K., et al. 2007, ApJ, 666, 1069
Maeda, K., Kawabata, K., Mazzali, P. A., et al. 2008, Sci, 319, 1220
Marion, G. H., Vinko, J., Kirshner, R. P., et al. 2014, ApJ, 781, 69
Maund, J. R., Smartt, S. J., Kudritzki, R. P., Podsiadlowski, P., & Gilmore, G. F. 2004, Natur, 427, 129
Maund, J. R., Fraser, M., Ergon, M., et al. 2011, ApJL, 739, L37
Maurer, I., Mazzali, P. A., Taubenberger, S., & Hachinger, S. 2010, MNRAS, 409, 1441
Mazzali, P. A., Kawabata, K. S., Maeda, K., et al. 2005, Sci, 308, 1284
McKinney, W. 2010, in Proc. 9th Python in Science Conf., ed. S. van der Walt & J. Millman, 61
McLeod, B., Fabricant, D., Nystrom, G., et al. 2012, PASP, 124, 1318
Meynet, G., & Maeder, A. 2005, A&A, 429, 581
Milisavljevic, D., Fesen, R. A., Gerardy, C. L., Kirshner, R. P., & Challis, P. 2010, ApJ, 709, 1343
Milisavljevic, D., Margutti, R., Soderberg, A. M., et al. 2013, ApJ, 767, 71
Miller, J. S., & Stone, R. P. S. 1994, The Kast Double Spectograph (Lick Observatory Technical Reports) (Univ. California Observatories/Lick Observatory)
Modjaz, M., Gutiérrez, C. P., & Arcavi, I. 2019, NatAs, 3, 717
Modjaz, M., Kirshner, R. P., Blondin, S., Challis, P., & Matheson, T. 2008, ApJL, 687, L9
Modjaz, M., Li, W., Butler, N., et al. 2009, ApJ, 702, 226
Mokiem, M. R., de Koter, A., Vink, J. S., et al. 2007, A&A, 473, 603
Monard, L. A. G. 2006, IAUC, 8666, 2
Munari, U., & Zwitter, T. 1997, A&A, 318, 269
Nadyozhin, D. K. 1994, ApJS, 92, 527
Nomoto, K., Tominaga, N., Umeda, H., Kobayashi, C., & Maeda, K. 2006, NuPhA, 777, 424
Oke, J. B., Cohen, J. G., Carr, M., et al. 1995, PASP, 107, 375
Parrent, J., Branch, D., Troxel, M. A., et al. 2007, PASP, 119, 135
Pastorello, A., Kasliwal, M. M., Crockett, R. M., et al. 2008, MNRAS, 389, 955
Pettini, M., & Pagel, B. E. J. 2004, MNRAS, 348, L59
Podsiadlowski, P., Joss, P. C., & Hsu, J. J. L. 1992, ApJ, 391, 246
Pogge, R. W., Atwood, B., Brewer, D. F., et al. 2010, Proc. SPIE, 7735, 77350A
Poznanski, D., Prochaska, J. X., & Bloom, J. S. 2012, MNRAS, 426, 1465
Prentice, S. J., & Mazzali, P. A. 2017, MNRAS, 469, 2672
Prentice, S. J., Ashall, C., James, P. A., et al. 2019, MNRAS, 485, 1559
Prochaska, J. X., Hennawi, J. F., Westfall, K. B., et al. 2020a, JOSS, 5, 2308
Prochaska, J. X., Hennawi, J., Cooke, R., et al. 2020b, pypeit/PypeIt: Release, v1.0.0, Zenodo, doi:10.5281/zenodo.3743493
Prochaska, J. X., Hennawi, J. F., Westfall, K. B., et al. 2020, JOSS, 5, 2308
Reichart, D., Nysewander, M., Moran, J., et al. 2005, NCimC, 28, 767
Sahu, D. K., Gurugubelli, U. K., Anupama, G. C., & Nomoto, K. 2011, MNRAS, 413, 2583
Salpeter, E. E. 1955, ApJ, 121, 161
Schlafly, E. F., & Finkbeiner, D. P. 2011, ApJ, 737, 103
Schlafly, E. F., Finkbeiner, D. P., Schlegel, D. J., et al. 2010, ApJ, 725, 1175
Science Software Branch at STScI, 2012 PyRAF: Python alternative for IRAF, Astrophysics Source Code Library, ascl:1207.011
Shahbandeh, M., Hsiao, E. Y., Ashall, C., et al. 2022, ApJ, 925, 175
Shigeyama, T., Nomoto, K., Tsujimoto, T., & Hashimoto, M.-A. 1990, ApJL, 361, L23
Shingles, L., Smith, K. W., Young, D. R., et al. 2021, TNSAN, 7, 1
Shivvers, I., Filippenko, A. V., Silverman, J. M., et al. 2019, MNRAS, 482, 1545
Silverman, J. M., Foley, R. J., Filippenko, A. V., et al. 2012, MNRAS, 425, 1789
Simcoe, R. A., Burgasser, A. J., Schechter, P. L., et al. 2013, PASP, 125, 270
Smith, K. W., Smartt, S. J., Young, D. R., et al. 2020, PASP, 132, 085002
Smith, M. P., Nordsieck, K. H., Burgh, E. B., et al. 2006, Proc. SPIE, 6269, 62692A
Smith, N., Li, W., Filippenko, A. V., & Chornock, R. 2011, MNRAS, 412, 1522
Stahl, B. E., Zheng, W., de Jaeger, T., et al. 2019, MNRAS, 490, 3882
Stetson, P. B. 1987, PASP, 99, 191
Stritzinger, M., Mazzali, P., Phillips, M. M., et al. 2009, ApJ, 696, 713
Stritzinger, M. D., Taddia, F., Burns, C. R., et al. 2018, A&A, 609, A135
Sukhbold, T., Ertl, T., Woosley, S. E., Brown, J. M., & Janka, H. T. 2016, ApJ, 821, 38
Sutherland, P. G., & Wheeler, J. C. 1984, ApJ, 280, 282
Taddia, F., Sollerman, J., Leloudas, G., et al. 2015, A&A, 574, A60
Taddia, F., Stritzinger, M. D., Bersten, M., et al. 2018, A&A, 609, A136
Tanaka, M., Tominaga, N., Nomoto, K., et al. 2009, ApJ, 692, 1131
Tartaglia, L., Fraser, M., Sand, D. J., et al. 2017, ApJL, 836, L12
Tartaglia, L., Sand, D. J., Valenti, S., et al. 2018, ApJ, 853, 62
Taubenberger, S., Valenti, S., Benetti, S., et al. 2009, MNRAS, 397, 677
Teffs, J., Ertl, T., Mazzali, P., Hachinger, S., & Janka, T. 2020, MNRAS, 492, 4369

Tody, D. 1986, Proc. SPIE, 627, 733
Tonry, J. L. 2011, PASP, 123, 58
Tonry, J. L., Stubbs, C. W., Lykke, K. R., et al. 2012, ApJ, 750, 99
Tonry, J. L., Denneau, L., Heinze, A. N., et al. 2018, PASP, 130, 064505
Tucker, M. A., Shappee, B. J., Huber, M. E., et al. 2022, PASP, 134, 124502
Tully, R. B., Rizzi, L., Shaya, E. J., et al. 2009, AJ, 138, 323
Uomoto, A. 1986, ApJL, 310, L35
Vacca, W. D., Cushing, M. C., & Rayner, J. T. 2003, PASP, 115, 389
Valenti, S., Benetti, S., Cappellaro, E., et al. 2008, MNRAS, 383, 1485
Valenti, S., Fraser, M., Benetti, S., et al. 2011, MNRAS, 416, 3138
Valenti, S., Sand, D., Pastorello, A., et al. 2014, MNRAS, 438, L101
Valenti, S., Howell, D. A., Stritzinger, M. D., et al. 2016, MNRAS, 459, 3939
Van Dyk, S. D., Li, W., Cenko, S. B., et al. 2011, ApJL, 741, L28
Van Dyk, S. D., Zheng, W., Fox, O. D., et al. 2014, AJ, 147, 37
Vink, J. S., de Koter, A., & Lamers, H. J. G. L. M. 2001, A&A, 369, 574
Virtanen, P., Gommers, R., Oliphant, T. E., et al. 2020, NatMe, 17, 261
Wang, S. Q., Wang, L. J., Dai, Z. G., & Wu, X. F. 2015, ApJ, 807, 147
Wellons, S., Soderberg, A. M., & Chevalier, R. A. 2012, ApJ, 752, 17
Wellstein, S., & Langer, N. 1999, A&A, 350, 148
Wheeler, J. C., & Harkness, R. P. 1990, RPPh, 53, 1467
Williamson, M., Modjaz, M., & Bianco, F. B. 2019, ApJL, 880, L22
Wilson, J. C., Henderson, C. P., Herter, T. L., et al. 2004, Proc. SPIE, 5492, 1295
Woosley, S. E. 2019, ApJ, 878, 49
Woosley, S. E., & Eastman, R. G. 1997, in Proc. NATO Advanced Study Institute 486, Thermonuclear Supernovae, ed. P. Ruiz-Lapuente, R. Canal, & J. Isern (Dordrecht: Kluwer), 821
Woosley, S. E., & Heger, A. 2007, PhR, 442, 269
Woosley, S. E., Heger, A., & Weaver, T. A. 2002, RvMP, 74, 1015
Woosley, S. E., Langer, N., & Weaver, T. A. 1993, ApJ, 411, 823
Woosley, S. E., Langer, N., & Weaver, T. A. 1995, ApJ, 448, 315
Woosley, S. E., Sukhbold, T., & Kasen, D. N. 2021, ApJ, 913, 145
Woosley, S. E., & Weaver, T. A. 1995, ApJS, 101, 181
Yoon, S.-C. 2015, PASA, 32, e015
Yoon, S.-C. 2017, MNRAS, 470, 3970
Yoon, S.-C., Chun, W., Tolstov, A., Blinnikov, S., & Dessart, L. 2019, ApJ, 872, 174
Yoon, S.-C., Dessart, L., & Clocchiatti, A. 2017, ApJ, 840, 10
Yoon, S. C., Woosley, S. E., & Langer, N. 2010, ApJ, 725, 940